ELSEVIER

Contents lists available at ScienceDirect

Ceramics International

journal homepage: www.elsevier.com/locate/ceramint





Unveiling the structure of calcium borate glass by neutron diffraction, MAS-NMR, Raman and first-principles calculations

Lulu Song ^{a,b}, Steve Feller ^c, Harry Hawbaker ^c, Wen Yin ^{d,e}, Wu Li ^a, Alex C. Hannon ^f, Yongquan Zhou ^a, Juping Xu ^{d,e}, Fayan Zhu ^{a,*}

- ^a Qinghai Institute of Salt Lakes, Chinese Academy of Sciences, Xining, 810008, China
- ^b University of Chinese Academy of Science, Beijing, 100049, China
- ^c Coe College, Physics Department, 1220 First Ave NE, Cedar Rapids, IA, 52402, USA
- ^d Institute of High Energy Physics, Chinese Academy of Sciences (CAS), Beijing, 100049, China
- e Spallation Neutron Source Science Center (SNSSC), Dongguan, 523803, China
- f ISIS Facility Rutherford Appleton Laboratory, Chilton, Didcot, Oxon, OX11 OQX, UK

ARTICLE INFO

Handling Editor: Dr P. Vincenzini

Keywords:
Calcium borate glass
Glass structure
Neutron diffraction
AIMD
Properties

ABSTRACT

Calcium borate glass is a challenging system, due to the rich variety of borate units and alterable boron coordination number, and hence they are also of particular interest for academic study. In this study, neutron diffraction, solid-state magic angle spinning nuclear magnetic resonance (MAS-NMR) and Raman spectroscopy were combined with first-principles calculations, experience potential structure refinement (EPSR) simulations to investigate the structure of xCaO·(1-x)¹¹B₂O₃ glass. Property data such as density and glass transition temperature were also measured to study the impact of structural changes on the properties of glasses. The structure of calcium borate glass was analyzed using various methods including structural unit, atomic pair bond length, coordination number, ring structure, chain structure and cavity distribution. Most notably, the atomic labeling method plays a key role in the structural analysis process. Through this method some new conclusions were obtained. For example, the increase of CaO content mainly leads to the conversion of BO to NBO in the glass structure, and has little effect on the content of BO3 and BØ4. This result further leads to an increase in Ca-NBO interactions. Interestingly, the bond length distribution of Ca-NBO and B-NBO is shorter than that of Ca-BO and B-BO, so the glass structure becomes denser. The structural reason why the density of calcium borate glass is less than the crystal density was also revealed. This study contributes to unveiling the structure of calcium borate glass and exploring the correlation between the structure and properties of calcium borate glass, which provides a valuable reference for developing more valuable amorphous materials.

1. Introduction

Amorphous materials are a special type of solid material that exhibits distinct solid characteristics. Their atomic structure is disordered, resembling that of a liquid and sometimes are referred to as "frozen liquids". Borate glass possess characteristics such as excellent linear optical response, energy dependence, and high sensitivity for low-dose radiation measurements. These properties meet the basic requirements for thermoluminescent materials, making them commonly used in the field of inorganic materials for thermoluminescence dose measurements [1]. Calcium borate glass has excellent bioactivity [2–4], which contributes to soft tissue repair [5,6], neuron survival rates [7], and bone

healing [8]. Dose detectors doped with calcium borate glass are expected to play a positive role in the treatment of bone cancer [9]. Calcium metaborate (CaB_2O_4) has the ability to enhance photoluminescence. The borate glass with embedded nano-sized $CaMoO_4$ microcrystals can be used as raw materials for photoluminescence applications [10–12]. Therefore, it can be seen that calcium borate glass has a wide range of application prospects.

The microscopic structure of amorphous materials at the atomic/molecule level determines their macroscopic properties. Krogh-Moe [13] suggested that the structure of borates glass consists of a random network structure as superstructural units. Bray [14,15] proposed that the superstructural units in the structure of borates glass are randomly

E-mail address: zhufayan@isl.ac.cn (F. Zhu).

^{*} Corresponding author.

connected to each other, and named this structure as the Warren-Zachariasen network. Alkaline-earth metal and alkali metal ions have a modifying effect on the borate network structure, changing the coordination number of boron atoms from 3 to 4 [16-19]. The conclusions of these studies provide references for us to analyze the $^{11}\mbox{B-MAS-NMR}$ spectra. Wright et al. [20] used neutron diffraction to study the structure of 0.29CaO·0.71B₂O₃ glass, and the atomic number density of this glass was found to be 0.09219 atom \mathring{A}^{-3} . They determined the average distance of Ca–Ca interaction in adjacent vacancies is $r_{\text{Ca-Ca}}$ = 4.25 \pm 0.09 Å. Ohtori et al. [21,22] conducted molecular dynamics simulations and neutron diffraction to study the structure of xCaO. $(1-x)^{11}B_2O_3(x = 0.20, 0.25, 0.33)$ glass. They found that the variation in the full width at half maximum (FWHM) of the first peak in the radial distribution function g(r) is related to the B–O coordination number of BO_4 unit. Kamitsos et al. [23] used infrared spectroscopy to estimate the content of B@4 in calcium borate glass structures. Their study revealed that as the content of CaO increases, the content of tetracoordinated boron (N_4) initially increases and then decreases, with the maximum value of N_4 occurring at $x \approx 0.45$. Maniu et al. [24] conducted Raman spectroscopy to study the structure of xCaO·(1-x)B₂O₃(0.20 < x < 0.60) glass and found that as the CaO content increases, the boron-oxygen six-membered rings transformed into six-membered rings containing BØ4, metaborate chains and rings, orthoborate units, and pyroborate units. Kamitsos et al. [25] suggested that the calcium borate glass formation range is within the range of xCaO·(1-x)B $_2$ O $_3$ (0.33 $\leq x \leq$ 0.50). They pointed out that the amorphous structure does not contain orthoborate units but includes metaborate-chains within this range. The network structure of borates is easily depolymerized by alkali metal cations. This depolymerization results in the transformation of bridging oxygen atoms (BO) into non-bridging oxygen atoms (NBO), and the formation of negatively charged BØ₄ tetrahedra to balance the positive charge of Ca²⁺ ions [26-28]. Nuclear magnetic resonance shows that there are three main types of boron atoms in borate glass: tetra-coordinated boron sites, axially symmetric tri-coordinated boron sites, and non-axially symmetric tri-coordinated boron sites [29-32]. The conclusion of this study provides a reference for us to analyze the ¹¹B-MAS-NMR spectra.

Many excellent results have been obtained for the structure of calcium borate glass, which provides a reference for the study of this paper. The microstructure of calcium borate glass still needs to be further studied, and much important information should be further discussed. For example, the data on the variations in bond lengths and coordination numbers of calcium borates glass (B-O, O-O, B-B, Ca-O, Ca-B, Ca-Ca) are not sufficiently complete. The effects of changes in atomic types (³B, ⁴B, BO, and NBO), structural units, and cavity structures on the physicochemical properties of glass (such as density and glass transition temperature) need to be clarified. Therefore, in this study, xCaO· $(1-x)^{11}$ B₂O₃(x = 0.27, 0.32, 0.37, 0.40, 0.42, 0.45, 0.49) glass were prepared using a nitrogen-protected melt-quenching method. Characterization was conducted by ICP, XRD, DSC, and solid density testing methods. Structural investigations were carried out using Raman spectroscopy, 11B-MAS-NMR, and neutron diffraction experiments, supplemented by CASTEP and AIMD simulation methods. We also use atomic labeling methods to study the interactions associated with ³B, ⁴B, BO, and NBO. The void distribution and ring structure in calcium borate glass were also analyzed. The difference between the structure of calcium borate glass and the crystal structure of similar components was also compared. This study further elucidates various structural details of calcium borates glass, providing valuable reference information for further research on borates glass.

2. Experimental

2.1. Sample preparation

At 800 °C, 99.96 % pure isotopically enriched boric acid (purity:

99.96 %, supplied by SIGMA-ALDRICH) was used to synthesize $^{11}\mathrm{B}_2\mathrm{O}_3$ glass. Using $^{11}\mathrm{B}_2\mathrm{O}_3$ glass and 99.0 % pure analytical-grade calcium carbonate (supplied by ChengDu Chron Chemicals Co,.Ltd) as raw materials, the melting container was a platinum crucible. The homogeneous and colorless transparent calcium borate glass systems with compositions of $x\mathrm{CaO}\cdot(1-x)^{11}\mathrm{B}_2\mathrm{O}_3$ (x=0.27, 0.32, 0.37, 0.40, 0.42, 0.45, 0.49) were prepared using a nitrogen-protected melt-quenching method. The samples were heated in a muffle furnace at 1400 °C for 20–30 min.

2.2. Samples characterization

The inductively coupled plasma atomic emission apectrometer (ICP-AES) was used to analyze the composition of the samples. The instrument model used was ICAP 6500 DUO. The experimental ratios and the results of quantitative elemental analysis are shown in Table 1. Density (iso) is the experimental density, and the relevant experimental conditions are shown in S1.3 of SI. The Density (iso) can be converted into density (nat) through formula calculation, so as to facilitate comparison with the density of literature. Atomic density and molar volume can also be calculated by formulas, all of which are shown in S1.3 of SI.

For specific details regarding the Raman spectroscopy, X-ray diffraction (XRD), density, and glass transition temperature experiments, please refer to the experimental section of the supplementary information. For density and Raman spectroscopy experiments, the samples were used in bulk, for neutron experiments, the samples were used in fine particles with a diameter of about 1 mm, and for ¹¹B-MAS NMR and glass transition temperature experiments, the samples were ground into a fine powder.

2.3. Neutron diffraction and 11B-MAS-NMR

ND: Neutron powder diffraction (NPD) experiments and neutron pair distribution function (nPDF) experiments were conducted on the Multi-Physics Instrument (MPI) [33] of the China Spallation Neutron Source (CSNS) in Dongguan, China. The powdered samples were sealed in cylindrical ZrTi alloy containers with a diameter of 8.9 mm inside a glove box filled with helium gas. The sealed containers were then placed in a vacuum diffraction chamber equipped with an automated sample changing environment. Measurements were performed using both the container filled with the 8.9 mm (diameter) × 30 mm (height) vanadium rod and an empty container as calibration references. The neutron wavelength range was 0.1 Å to 4.5 Å, with an optimal O-resolution of 0.3 %. The total diffraction data was processed using the Mantid program [34] to perform sample non-diffraction correction. The data were then normalized using vanadium and converted to the S(Q) function. The merged simplified structure function within the Q range of 1.05 Å to 31.4 Å was Fourier transformed to obtain the nPDF data.

The formula for calculating the pair distribution function g(r) is as follows:

$$g(r) = \frac{\rho(r)}{\rho_0} = 1 + \frac{1}{2\pi^2 \rho_0 r} \int_0^\infty Q[S(Q) - 1] \sin(Qr) dQ \tag{1}$$

This algorithm is implemented through the following equation:

$$g(r)-1=\frac{1}{2\pi^2\rho_0r^3}\sum_{Q_{min}}^{Q_{max}}M(Q,Q_{max})[S(Q)-1][\sin(Qr)-Qrcos(Qr)]_{leftbin}^{rightbin} \eqno(2)$$

Among them, M (Q, Q_{max}) is an optional filtering function. If the Filter property is set to true, then:

$$M(Q,Q_{max}) = \frac{\sin (\pi Q/Q_{max})}{\pi Q/Q_{max}}$$
(3)

Otherwise:

$$M(Q,Q_{max}) = 1 \tag{4}$$

Table 1
The composition, $R = \text{CaO(mol)}/^{11}\text{B}_2\text{O}_3(\text{mol})$, mass density, atomic density, molar volume and glass transition temperature of calcium borate glass.

Preparation ratio		ICP results		x	R	Density (iso.)	Density (nat.)	Atom density	$V_{ m m}$	T_{g}
CaO (mol)	¹¹ B ₂ O ₃ (mol)	CaO (mol)	¹¹ B ₂ O ₃ (mol)			(g·cm ⁻³)	(g·cm ⁻³)	(Å ⁻³)	(mol·cm ⁻³)	(°C)
0.26	0.74	0.26 (0.01)	0.74 (0.01)	0.27	0.36	2.48 (0.0114)	2.47 (0.0140)	0.095 (0.0004)	26.71 (0.12)	652.80 (3.26)
0.33	0.67	0.32 (0.01)	0.68 (0.01)	0.32	0.47	2.51 (0.0153)	2.50 (0.0082)	0.093 (0.0004)	26.11 (0.12)	651.17 (3.26)
0.39	0.61	0.37 (0.02)	0.63 (0.02)	0.37	0.59	2.58 (0.0187)	2.57 (0.0232)	0.093 (0.0007)	25.1 (0.10)	649.87 (3.25)
0.42	0.58	0.40 (0.02)	0.60 (0.02)	0.4	0.66	2.64 (0.0094)	2.63 (0.0019)	0.094 (0.0001)	24.44 (0.03)	643.93 (3.22)
0.45	0.55	0.42 (0.03)	0.58 (0.03)	0.42	0.72	2.67 (0.0120)	2.66 (0.0084)	0.094 (0.0001)	24.05 (0.03)	638.99 (3.19)
0.50	0.50	0.45 (0.05)	0.55 (0.05)	0.45	0.82	2.73 (0.0160)	2.72 (0.0063)	0.094 (0.0040)	23.35 (0.11)	625.41 (3.13)
0.53	0.47	0.49 (0.04)	0.51 (0.04)	0.49	0.97	2.76 (0.0131)	2.75 (0.0156)	0.093 (0.0030)	22.88 (0.07)	616.65 (3.08)

^{*} Density (iso.) is the density of the isotope boron glass, Density (nat.) represents the density of natural boron glass.

The formula for calculating the total pair distribution function is as follows:

$$G(r) = 4\pi \rho_0 r[g(r) - 1] \tag{5}$$

 $^{11}\mbox{B-MAS-NMR}$: The $^{11}\mbox{B-MAS}$ solid-state nuclear magnetic resonance experiments on calcium borate glass were conducted using a Bruker 600 MHz (14.1 T) solid-state NMR instrument (Model: Bruker AVANCE NEO 600 MHz). The powder glass sample was loaded into a 4 mm ZrO2 rotor inside a glove box filled with argon gas, and sealed with a Kel-F cap. The nuclear magnetic resonance spectrum was acquired at a magnetic field strength of 192.568 MHz using an HX dual-channel probe. The measurements were conducted at a temperature of 300 K, with a rotor spinning frequency of 20 Hz and a magic angle spinning frequency of 11.5 KHz. The obtained spectrum had a resolution of 2.3475 Hz.

2.4. 11B-MAS- NMR spectrum analysis method

The ¹¹B MAS NMR spectra were analyzed using the dmfit program [35]. Tri-coordinated boron sites (³B) with large C_Q values (typically around 2.6 MHz) result in significant second-order quadrupolar broadening, leading to a reduction in the resolution of the ¹¹B MAS spectrum [31]. Therefore, during the analysis, fitting is performed by using Q mas 1/2 and adjusting the quadrupolar coupling constant (C_Q) and asymmetry parameter (η). The peaks corresponding to tetra-coordinated boron sites (⁴B) exhibit sharp profiles. The analysis is performed using a Gaus/Lor function, and the parameter xG/(1-x) L (Gaussian/Lorentzian ratio, where G represents Gaussian and L represents Lorentzian) is adjusted accordingly.

The Raman spectroscopy analysis methods can be found in the Raman spectroscopy analysis section of the Supplementary Information.

2.5. Ab initio molecular dynamics simulation

Ab initio molecular dynamics simulation (AIMD) were performed on the Ca-borate glass structure using the Born-Oppenheimer molecular dynamics method and the CP2K package [36]. The generalized gradient approximation (GGA) and the Perdew-Burke-Ernzerhof (PBE) functional were applied in the simulations [37]. The initial atomic configuration of the glassy calcium borate was generated using the packmol software [38]. The cubic simulation boxes at room temperature contained approximately 400 atoms (depending on the composition of each sample) to match the experimental density. The size and number of atoms in each simulation box are shown in Table S4. Density functional theory (DFT) was employed for further optimization, utilizing the consistent-polarized double-ζ valence basis set DZVP [39,40] for each involved atom, as well as Goedecker-Teter-Hutter (GTH) pseudopotentials [41]. After DFT optimization, the AIMD simulations were carried out in a typical NVT ensemble using a Nosé-Hoover thermostat [42, 43] with a length of 3, and a time step of 1 fs/step. First, it balances 20 ps at 298.15 K, and then heats up to balance 10ps at 698.15K and 1198.15K, respectively. 1198.15K is already higher than the glass

transition temperature (~925K), but the structure still has defects. To obtain more reasonable simulation results, the maximum temperature was raised to 1398.15K and equilibrated for 20 ps. It was then cooled to 298.15 K through the same temperature gradient and similar simulation time. Finally the simulation was equilibrated for 20 ps, then the data were collected. Connectivity and ring statistics were analyzed using R.I. N.G.S [44]. The pore distribution was analyzed using the pyMolDyn program [45].

The detailed calculation of the Raman spectra of the crystals is in the CASTEP calculation section of SI.

2.6. Refinement of empirical potential structure

The empirical potential structure refinement (EPSR) method is used to analyze the neutron diffraction experimental data of calcium borate glass. EPSR [46] is a method that can generate physically reasonable atomic models of condensed amorphous systems that are consistent with total diffraction data. The model adopts a reference potential consisting of standard Lennard-Jones plus coulomb terms. When constructing the model, about 4000 atoms (Ca, B, O atoms) are placed in a cubic box with periodic boundary conditions. Table 2 lists the Lennard Jones potential parameters, and the atomic charges, box composition, and size are listed in Table S3. Before the EPSR, after equilibrating at 10,000K, the initial structure model is obtained by continuous NVT Monte Carlo equilibration under the reference potential through a continuous cooling process of 1400K, 1200K, 1000K, 700K, 300K. The structural parameters and their distribution structure are the average of a series of configurations, because they fluctuate around the final equilibrium energy. At the final equilibrium energy, the model and the experimental diffraction cross-section are in good agreement.

3. Results and discussion

3.1. Raman spectra

The Raman spectra of calcium borate glass xCaO·(1-x) 11 B₂O₃ $(0.26 \le x \le 0.49)$ are shown in Fig. 1. For x = 0.26, the main peak at 778 cm $^{-1}$ is due to the breathing mode of a six-membered ring containing one BØ4 tetrahedral unit [25,47]. As the content of CaO increases, this peak was red-shifted to 765 cm $^{-1}$, and the corresponding structural unit transitions to a six-membered ring containing two BØ4 tetrahedra. As the content of CaO increases, the peak at 661 cm $^{-1}$ was blue shifted to \sim 677 cm $^{-1}$ which represents the metaborate chains [25]. The peak at

Table 2
Lennard Jones potential parameters.

Atom Type	Lennard Jones Parameters						
	Epsilon(kJ/mol)	Sigma(Å)	AW (amu)				
¹¹ B	0.1750	0.5000	11.0000				
0	0.1625	3.6000	16.0000				
Ca	0.4185	2.9850	40.0000				

^{*} The data in brackets represents the error value.

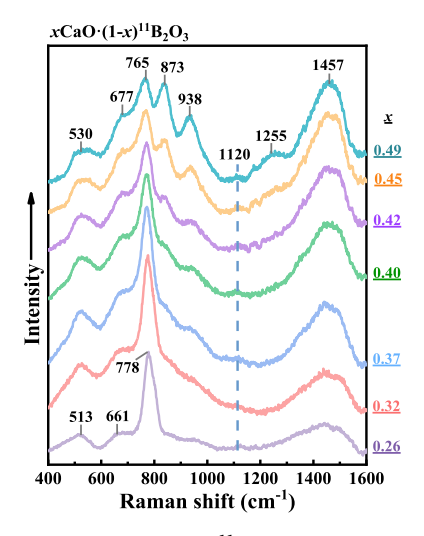


Fig. 1. Raman spectra of xCaO· $(1-x)^{11}$ B₂O₃ glasses, for $0.26 \le x \le 0.49$.

1300-1600 cm⁻¹ is the stretching vibration of the terminal B–O bond in the structural unit, its content was used to represent the content of ionic structural units in the entire system [48,49].

As the content of CaO increases, a shoulder peak gradually appears on the right side of \sim 770 cm⁻¹. When x = 0.42, the intensity of this peak gradually increases, and the peak position was blue-shifted from 837 ${\rm cm}^{-1}$ (x = 0.37) to 873 cm⁻¹ (x = 0.49), the peak is attributed to the vibration of the B-O-B bridge in the pyroborate unit [47]. The peak at 940 cm⁻¹ also gradually strengthens with the increase in CaO content. Maniu et al. [24] reports that this peak belongs to the orthoborate unit. while Kamitsos et al. [25,50] suggests that this peak belongs to other structural units containing BØ4 tetrahedra. In this study, the cell structure of similar component crystals and corresponding Raman spectrum were calculated using CASTEP (see section 2.3.3), as shown in Fig. S2 (a) \sim (d). The peak at \sim 940 cm⁻¹ is related to the stretching vibration of the central boron atom in B \emptyset_4 tetrahedra, and the peak at ~947 cm⁻¹ in the Raman spectrum of CaB₄O₇ crystal (Fig. S2 (b)) is attributed to the diborate group containing two BØ4 tetrahedra. Therefore, the peak at \sim 940 cm⁻¹ is attributed to the diborate group. It is worth mentioning that, based on the results of our CASTEP study (Fig. S2 (b)), we attribute

the $1120~{\rm cm}^{-1}$ vibration peak, which was not clearly assigned by previous researchers, to the symmetric stretching vibration of the B–O–B bridge in the diborate group. This result further indicates that diborate groups definitely exist in calcium borate glass. The details of the Raman spectrum are shown in Table S2.

The peaks in the Raman spectrum were fitted using Gaussian and Lorentzian functions, as shown in Fig. 2 (left) and Fig. S3. When x=0.26, there is no obvious characteristic peak of boroxol ring in the Raman spectrum. However, there is a less visible shoulder to the right of the main peak 778 cm $^{-1}$. This shoulder peak corresponds to the boroxol ring which is disappeared when $x\geq0.32$. Maniu et al. [24] suggested that when x=0.20, there was an obvious boroxol ring peak, and when x=0.40, the peak was located on the shoulder of the main peak, and when x=0.40, the peak disappeared, which was similar to the results of this study. The boroxol ring in lithium borate glass exists at x=0.20, and has disappeared when $x\geq0.26$ [51], which also indicates that the modification ability of Ca^{2+} on B_2O_3 glass is stronger than that of Li^+ .

Fig. 2 (right) shows the relative content change curve of each structural unit. As shown in the figure, x=0.32 and 0.42 are two important inflection points where the structural units undergo significant changes. When $0.26 \le x \le 0.32$, the ring structure units (the sixmembered ring including one BØ4 tetrahedra) are transformed into, the long-chain structure units (metaborate-chains) and short-chains structure units (pyroborate units). The decreasing trend of ring structure units is similar to the result reported by Maniu et al. [24]. When $0.32 < x \le 0.42$, the content of each structural unit changes little but still maintains the trend of the reduction of ring structure unit and increase of chain structure units. When $0.42 < x \le 0.49$, the long-chain and six-membered ring structural units are converted to the short-chain structural units with more NBO and diborate groups, and the content of various structural units varied greatly.

3.2. ¹¹B MAS-NMR

Fig. 3 shows the ¹¹B MAS NMR spectrum of calcium borate glass. The spectrum was analyzed using the dmfit program [35], resulting in three different boron sites: (1) tetra-coordinated boron site with a quadrupolar coupling constant (C_Q) less than 1 MHz and a chemical shift close to 0 ppm; (2) Axially symmetric tri-coordinated boron site ($C_Q \approx 2.4-2.7$ MHz) with an asymmetry parameter (η) less than 0.5; (3) Non-axially

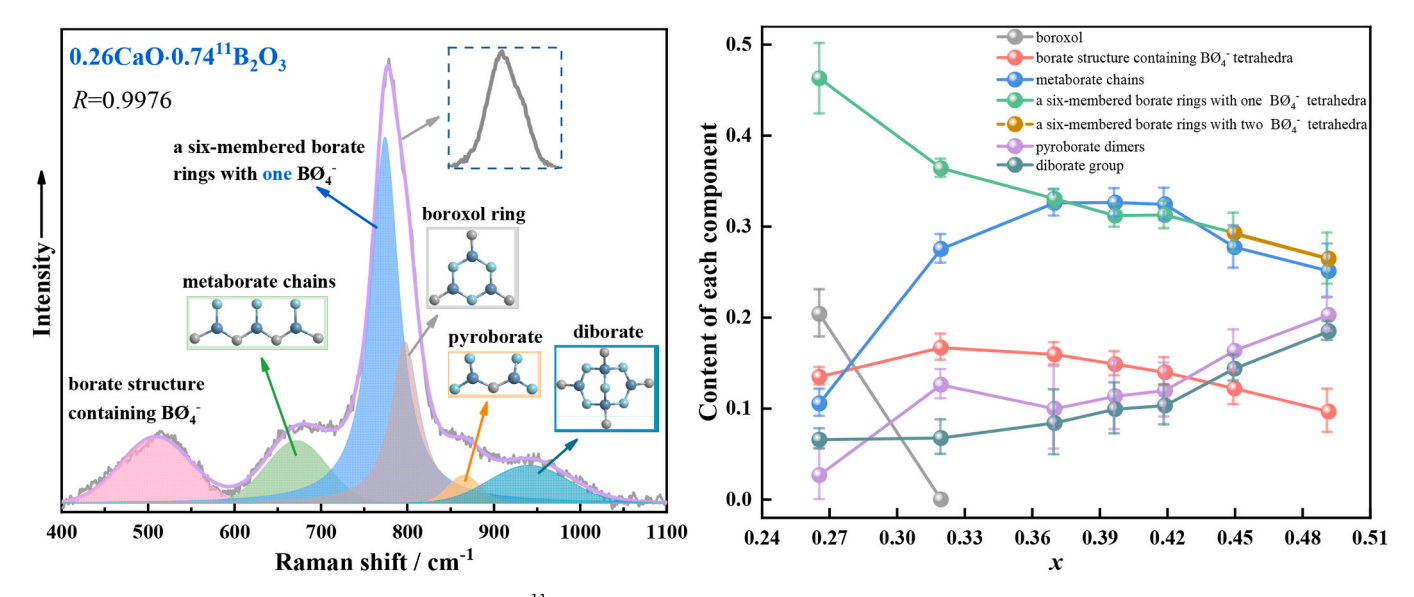


Fig. 2. Left, experimental and fitted spectra of 0.26CaO· 0.74^{11} B₂O₃ glass: the gray lines are the experimental Raman spectra, the purple lines are the total spectra of the fitted spectral components, colored skeleton maps are the fitted spectral components; R is the coefficient of determination. Right, the relationship between the relative content of each structural unit in the calcium borate glass and the content of CaO value. (For interpretation of the references to color in this figure legend, the reader is referred to the Web version of this article.)

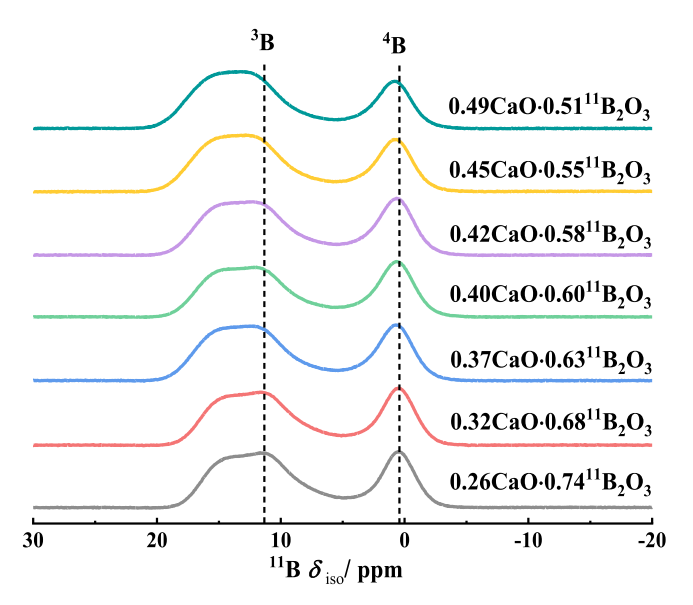


Fig. 3. 11 B MAS NMR spectrum of xCaO·(1-x) 11 B $_2$ O $_3$ glasses, for $0.26 \le x \le 0.49$.

symmetric tri-coordinated boron site ($C_Q \approx 2.5$ –3.0 MHz, with η greater than 0.5). This distribution is similar to the distribution of boron sites in sodium borate, barium borate and lead borate glass [30,52,53]. The low η site corresponds to tri-coordinated boron with three BO or three NBO, while the high η site corresponds to tri-coordinated boron containing one or two NBO, as shown in Fig. 4 and Fig. S4.

Percentage change of three and four coordinated boron, symmetric and asymmetric three coordinated boron are shown in Fig. 5. From the graph, it can be observed that the content of symmetrically tricoordinated boron decreases linearly with the increase of CaO. Raman spectroscopy also shows that there are no orthoborate units. Therefore, in the symmetric 3B site, there are no 3B site that contain three NBOs. The decrease in N_{3S} suggests a reduction in structures containing three BO. On the other hand, the content of non-symmetrically tri-coordinated boron linearly increases, indicating a gradual increase of structures containing one or two NBO units. The change of the structural units involved NBOs are pyroborate units and metaborate-chains as shown in Fig. 2 right. The N_4 has little change, the structural units containing BO_4 tetrahedra are mainly composed of diborate groups and six-membered ring which contains one or two BO_4 tetrahedra. Therefore, the

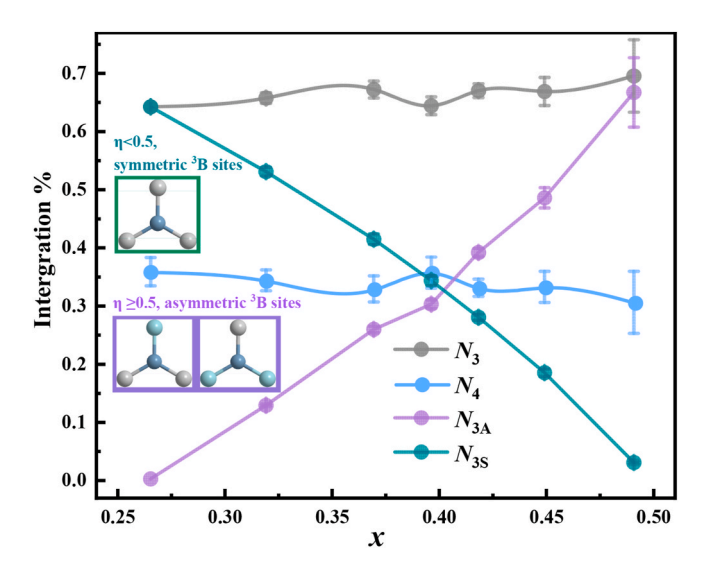


Fig. 5. Percentage change of tri- and tetra-coordinated boron, symmetric and asymmetric tricoordinate boron content changes.

increase of N_4 can't balance the positive charge from Ca^{2+} , leading to an increase content of NBO. Additionally, a maximum point of N_4 appears around x=0.40, and Fig. 2 (right) also shows that the content of sixmembered ring containing one BO_4 tetrahedron and other structural units containing BO_4 tetrahedra is relatively high around x=0.40. This maximum point is consistent with research conclusion obtained by Feller et al. [54]. At the same time, this extreme point is approximate to the N_4 maximum point (x=0.38) given by Wu et al. [55,56]. In crystals such as CaB_6O_{10} , CaB_4O_7 , $Ca_2B_6O_{11}$, and CaB_2O_4 , the crystal with the highest N_4 is $Ca_2B_6O_{11}$ (with a molar content of CaO of 0.40) as shown in Fig. S10. Therefore, $x\approx0.40$ is a turning point where the structure undergoes significant changes.

3.3. Analysis of neutron diffraction experimental results

Fig. 6 (left) shows the total-scattering structure factor F(Q) of xCaO· $(1-x)^{11}$ B₂O₃ $(0.26 \le x \le 0.49)$ glasses. it also provides the F(Q) of 11 B₂O₃ obtained from China Spallation Neutron Source (CSNS) and the ISIS Neutron and Muon Source (11 B₂O₃-CSNS and 11 B₂O₃-ISIS, respectively). the peak shapes and positions of 11 B₂O₃-CSNS and 11 B₂O₃-ISIS are very similar, indicating that high-quality experimental data have been

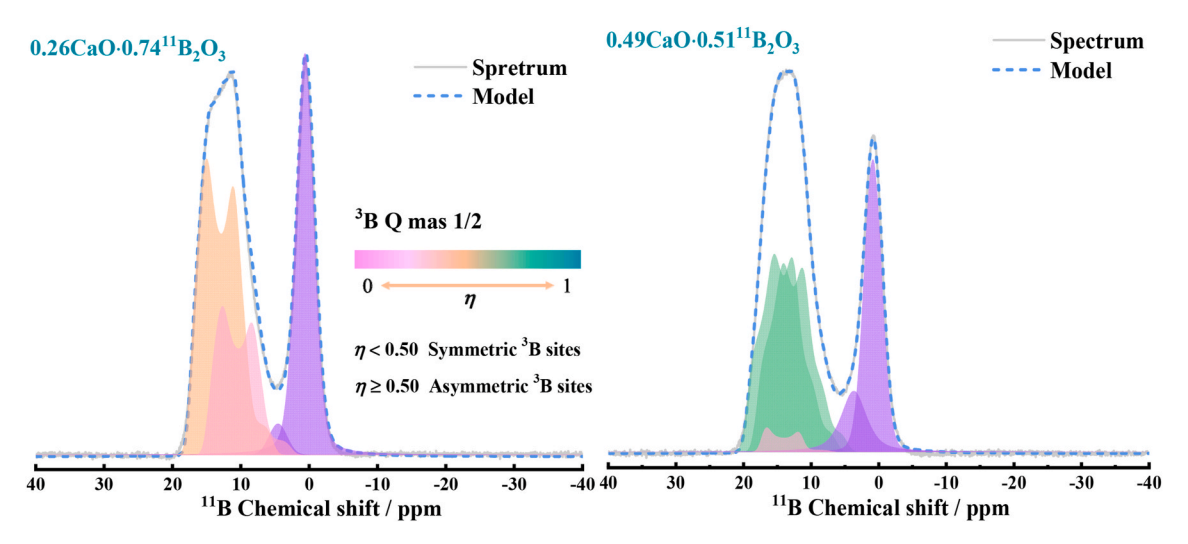


Fig. 4. 11 B MAS NMR models of xCaO·(1-x) 11 B₂O₃ glasses. Changes in the color axis are used to indicate the size of η . (For interpretation of the references to color in this figure legend, the reader is referred to the Web version of this article.)

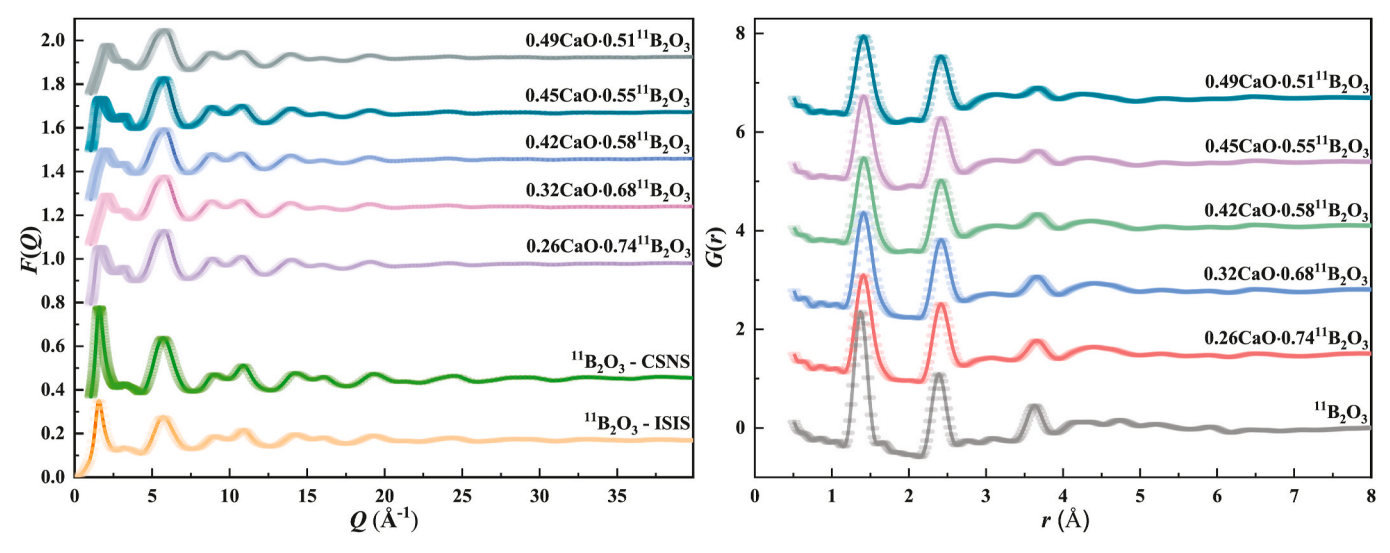


Fig. 6. Left: the total-scattering structure factor F(Q) of calcium borate glass, ${}^{11}B_2O_3$ -CSNS and ${}^{11}B_2O_3$ -ISIS represent scattering data from China Spallation Neutron Source (CSNS)and ISIS Neutron and Muon Source (ISIS), respectively. Right: the total radial distribution function G(r) of calcium borate glass. Error bars (Short and light colored lines) have been added to all data.

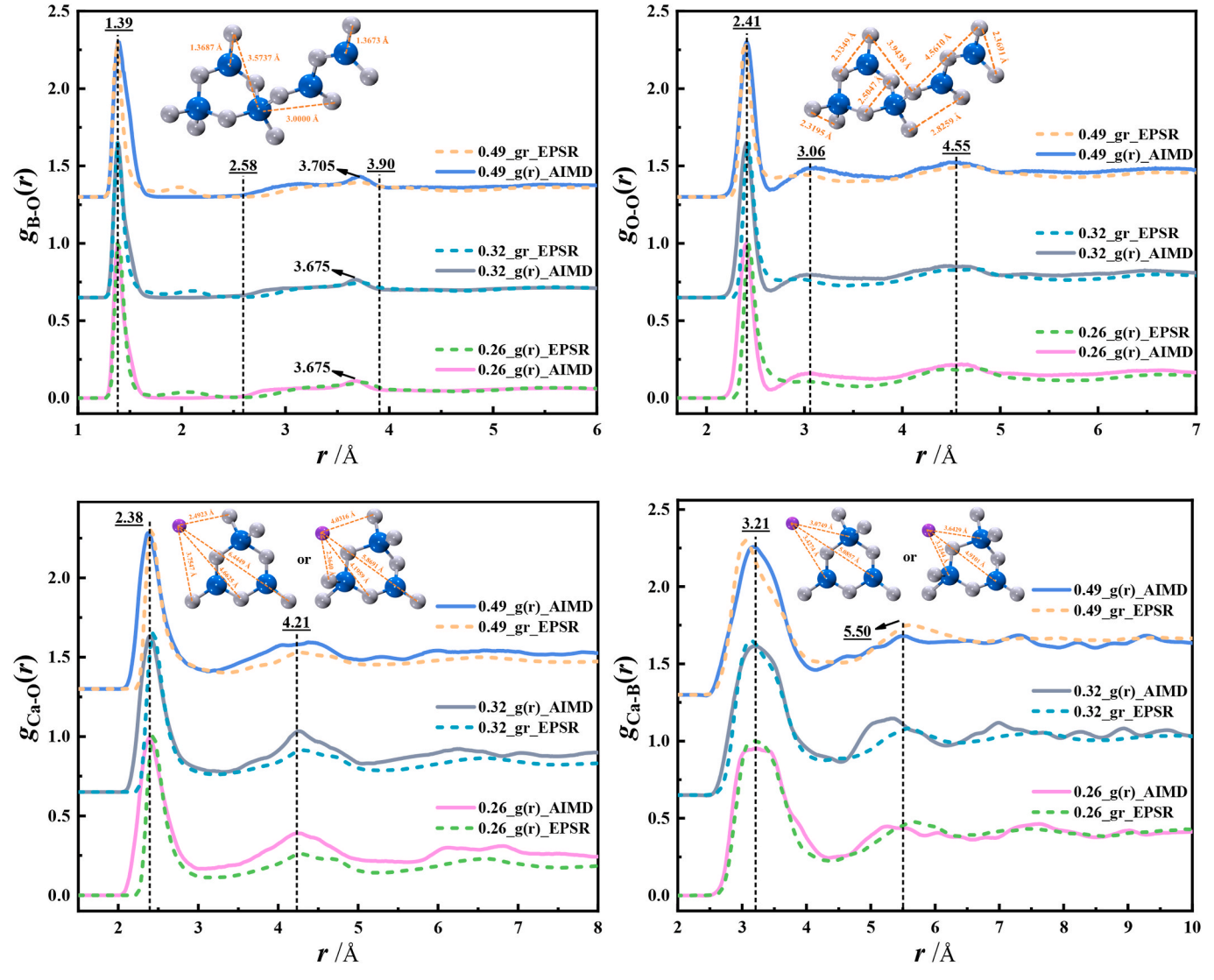


Fig. 7. Partial pair distribution function of xCaO· $(1-x)^{11}$ B₂O₃ (0.26 $\leq x \leq 0.49$) glass obtained by EPSR and AIMD methods.

obtained at CSNS. the first sharp diffraction peak (FSDP) of F(Q) and the glass transition temperature (T_g) are closely related to the medium-range order of the glass structure [57]. Specifically, as the CaO content increases, the intensity of the FSDP gradually weakens, and T_g decreases (as shown in Table 1), indicating an increase in the medium-range order of calcium borate glass.

The total radial distribution function G(r) is shown in Fig. 6 (right). Three peaks observed in the graph, located at approximately 1.41, 2.41 and 3.65 Å. The peak at 1.41 Å corresponds to the B–O interaction. The peak at around 2.41 Å corresponds to the O–O interaction within BO₃ and BØ̄4 units, the B–B interactions in adjacent structural units, as well as the B–O interaction in the second nearest neighbor. The peak at 3.65 Å represents interactions such as Ca–O, Ca–B, and the B–O and O–O interactions in the second nearest neighbor.

3.4. Analysis of neutron diffraction experiment data

3.4.1. Pair distribution function (PDF) and coordination number (CN)

The experimental and EPSR simulated spectra of F(Q) and G(r) are shown in Fig. S5. From the graph, it can be observed that the EPSR simulated F(Q) and G(r) data exhibit good overlap with the neutron experimental data, indicating the reliability of the EPSR simulation results. The AIMD method was also used to verify the EPSR simulation as shown in Fig. 7. There is a slight difference in the PDF data obtained by using these two methods. EPSR is based on Monte Carlo simulations, while AIMD is based on first-principles calculations. The underlying theories and methodologies of these two approaches are leading to variations in the obtained results. The size of the simulation boxes can also influence the simulation results. In EPSR simulations, the number of atoms in the simulation box is around 4000, which is approximately 10 times larger than the number of atoms in the AIMD simulation box. Based on the observation that the peak positions in the PDF spectra obtained from AIMD and EPSR simulations are roughly similar, especially the first coordination shells exhibit good overlap. Therefore, AIMD simulation results were mainly used to analyze the results. We used different AIMD methods and different calculation temperatures to determine more suitable calculation conditions, as shown in the AIMD section of SI for details. The calculation results showed that the calculation method and temperature given in the manuscript are suitable.

The makex, xtal and Open Genie programs [58–60] were used to calculate the PDF of calcium borate crystals such as CaB_6O_{10} , CaB_4O_7 , $Ca_2B_6O_{11}$, and CaB_2O_4 as shown in Fig. 8 and S9. Both NBO and BO interactions exist in the CaB_2O_4 crystal, while only BO interactions are present in CaB_6O_{10} , CaB_4O_7 , and $Ca_2B_6O_{11}$ crystals. Fig. 9 displays the coordination number distribution of the first coordination shells of B–O,

Ca-O, and O-O interactions in calcium borate glass and crystals.

3.4.1.1. B-O interaction. As shown in Fig. 7, the first coordination shell distance of B–O interaction r_{B-O} is 1.39 Å. Ohtori et al. [61] suggested the r_{B-O} ranges from 1.37 to 1.38 Å. These values are in close agreement with present results. The second coordination shell of the B-O interaction is observed between 2.58 and 3.90 Å. This second coordination shell includes various interactions such as B-O interactions within six-membered rings, B-O interactions between the six-membered ring and neighboring BO3 or BØ4 units, and B-O interactions between BO3 and BO₃ or BØ₄ units. Ohtori et al. [61] reported that the distances for the second coordination shell of B-O interaction were 3.71, 3.72, and 3.70 Å, which is in close agreement with present study. With an increase in CaO content, the first coordination shell bond length of B-O showed minor changes (as shown in Table S5), while the peak half-width significantly increased and the asymmetry of the peaks enhanced. Ohtori et al. [21] suggested that the asymmetry of the B-O interaction peak is related to the content of BO₃ and BØ₄. The coordination number of B-O involving BO₃ and BØ₄ does not change significantly as shown in Fig. 5. However, there are noticeable changes in the content of symmetric tri-coordinated boron (containing BO) and asymmetric boron (containing one or two NBO). Therefore, the variation of BO and NBO in the amorphous structure also affects the symmetry of B-O interaction peak.

In order to elucidate the reasons for the asymmetry of the B–O interaction peaks mentioned above, we further investigated the effects of 3 B, 4 B, BO, and NBO on the B–O interaction with the increase of CaO content. The four groups of atoms in the equilibrium structures were labeled as 3 B-BO, 3 B-NBO, 4 B-BO, and 4 B-NBO. The same labeling method was used to the CaB $_3$ O $_4$ crystal containing both BO and NBO as shown in Fig. 10. The bond length and relative content of each interaction are shown in Table S8. The graph reveals significant differences between the structure of the glass and the crystal with similar compositions. These differences include:

- (1) In the 0.49CaO· 0.51^{11} B₂O₃ glass, the percentage of 4 B-NBO interactions is approximately 2.6 %, these are absent in the CaB₃O₄ crystal.
- (2) The dominant B–O interaction in the $0.49\text{CaO} \cdot 0.51^{11}\text{B}_2\text{O}_3$ glass is $^3\text{B-BO}$, approximately 39.4 %, whereas in the CaB_3O_4 crystal, the dominant interaction is $^4\text{B-BO}$ interactions, approximately 55.0 %.
- (3) The bond lengths of 3 B-BO in the 0.49CaO·0.51 11 B₂O₃ glass and CaB₃O₄ crystal are approximately 1.41 Å and 1.45 Å, respectively.

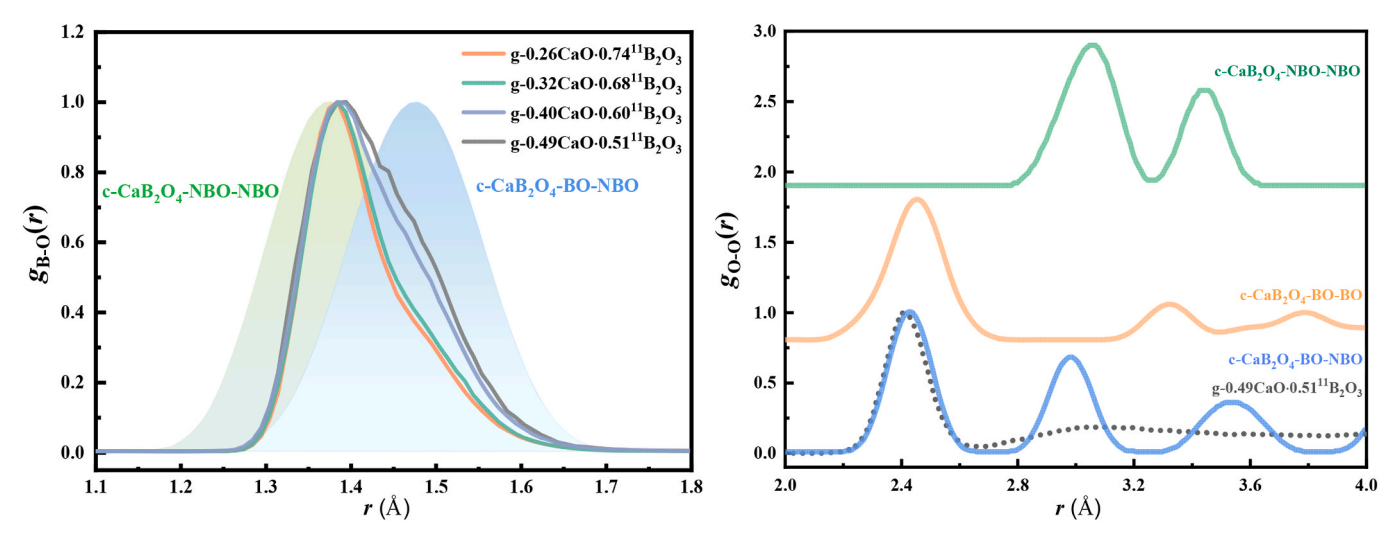


Fig. 8. Partial pair distribution function of xCaO· $(1-x)^{11}$ B $_2$ O $_3$ (0.26 $\leq x \leq$ 0.49) glasses and CaB $_2$ O $_4$ crystal.

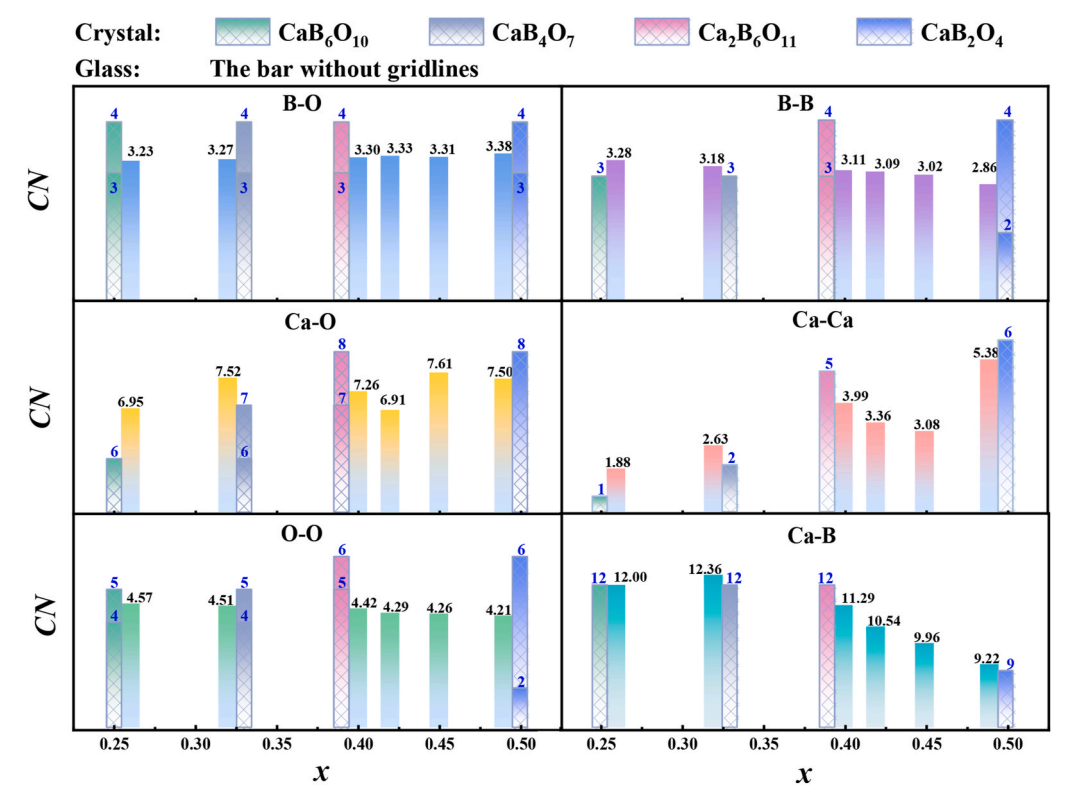


Fig. 9. Coordination number of the first coordination layer of xCaO·(1-x) 11 B₂O₃ (0.26 $\le x \le 0.49$) glass and CaB₆O₁₀, CaB₄O₇, Ca₂B₆O₁₁, CaB₂O₄ crystals.

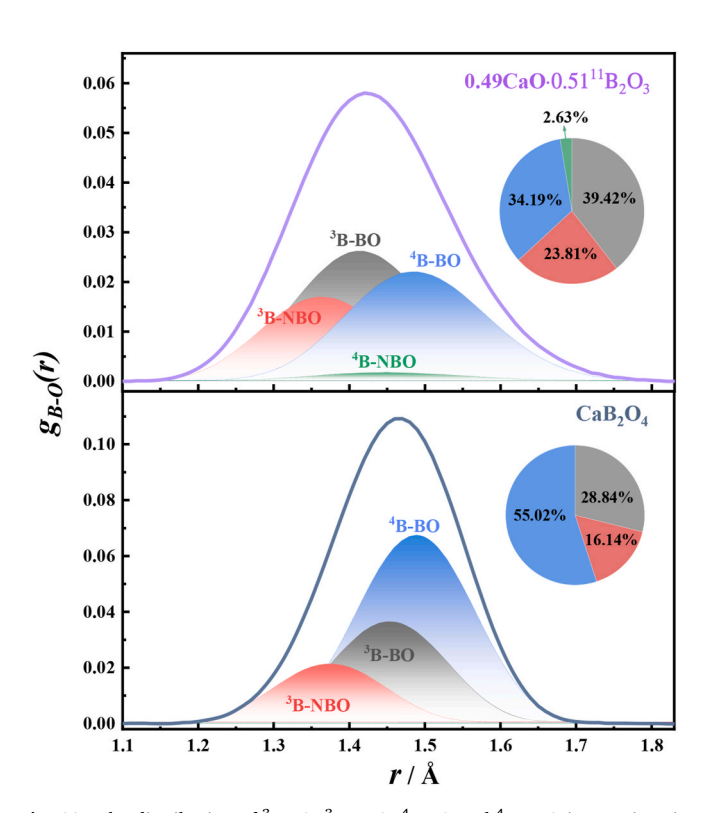


Fig. 10. The distribution of 3B -BO, 3B -BO, 4B -BO and 4B -NBO interactions in the first coordination layer of the B–O interaction in 0.49CaO-0.51 $^{11}B_2O_3$ glass and CaB $_2O_4$ crystal, the fan chart on the right shows the percentage of each atom-pair interaction.

Furthermore, there are also similarities in the structures of the mentioned glasses and crystals. The $^3B\text{-NBO}$ bond length in glass and similar composition crystals is almost the same, about 1.37 Å, and the $^4B\text{-BO}$ bond length is also very close, about 1.49 Å. Wright et al. [20] obtained B–O interaction distances of approximately 1.37 Å and 1.46 Å for BØ₃ and BØ₄ structures, respectively, in the 0.28CaO-0.72B₂O₃ glass by neutron diffraction method. In this work, $r_{3B\text{-NBO}}\approx 1.37$ Å and $r_{4B\text{-NBO}}\approx 1.48$ Å in 0.26CaO-0.74 11 B₂O₃ glass, $r_{3B\text{-NBO}}\approx 1.37$ Å and $r_{4B\text{-NBO}}\approx 1.47$ Å in 0.32CaO-0.68 11 B₂O₃ glass, which are similar to the results from Wright et al.

The relative abundances of ³B-BO, ³B-NBO, ⁴B-BO, and ⁴B-NBO interactions in the amorphous phase, as well as their variation with

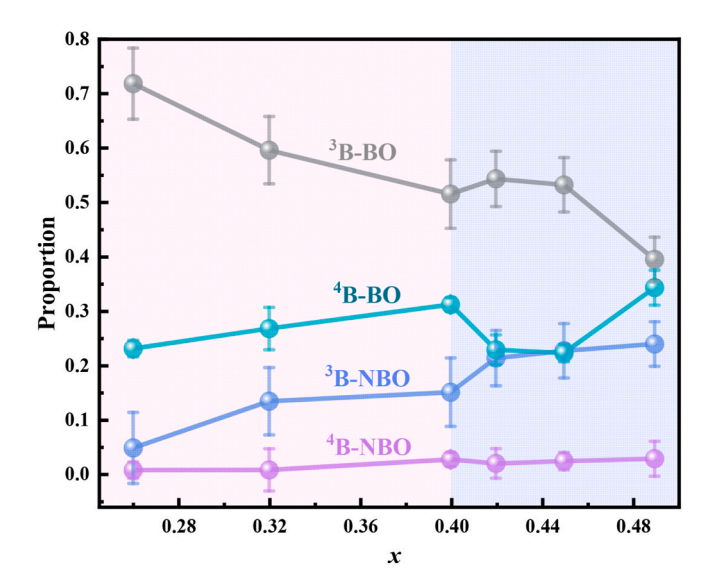


Fig. 11. The relative contents of ${}^3\text{B-BO}$, ${}^3\text{B-NBO}$, ${}^4\text{B-BO}$ and ${}^4\text{B-NBO}$ interaction in $x\text{CaO}\cdot(1\text{-}x)^{11}\text{B}_2\text{O}_3$ (0.26 $\leq x \leq$ 0.49) glass.

composition, are shown in Fig. 11. The most abundant interaction is ³B-BO, followed by ⁴B-BO and ³B-NBO interactions. The variation of CaO content has a minimal impact on the abundance of ⁴B-NBO interactions. At $0.26 \le x \le 0.40$, with an increase in CaO content, the abundance of ³B-BO interactions decreases, while the abundances of ³B-NBO and ⁴B-BO interactions increase. At $0.40 \le x \le 0.49$, the content of ³B-BO interactions initially increases and then decreases, the content of ⁴B-BO interactions first decreases and then increases, and the content of ³B-NBO interactions increases. Therefore, x = 0.40 represents a turning point for the variations in the four types of interactions. The turning point coincides with the peak of N_4 , and it is also very close to the intersection where the content of symmetric tri-coordinated boron with three BO interactions and asymmetric tri-coordinated boron with one or two NBO interactions changes (as shown in Fig. 5). The structural units' changes (Fig. 2 right) indicate that the six-membered ring containing BØ4 and metaborate-chains transform into pyroborate units and diborate groups when x > 0.40. The bond length for ³B-BO, ³B-NBO, ⁴B-BO, and ⁴B-NBO interactions are shown in Table S8. Each type of B-O interaction exhibits a turning point in bond length at x = 0.40, indicating a significant structural change, which is consistent with the results in Fig. 2 (right graph). The contents of BO and NBO in each component are shown in Fig. S11. As the CaO content increases, the content of BO gradually decreases, while the content of NBO increases. The content of BO remains higher than that of NBO. The results of ¹¹B-MAS-NMR (Fig. 5) also indicate a decrease in the content of symmetric tri-coordinated boron with three BO interactions and an increase in the content of asymmetric boron sites with one or two NBO interactions as the CaO content increases. This phenomenon is consistent with the results in Fig. S11. The above research indicates that with an increase in CaO content, the NBO content increases, and the network structure of calcium borate glass is dispersed, forming numerous "molecular-type" rings and chain structures containing NBO. When x = 0.40, the structure of calcium borate glass is the most dispersed, the short chain structure containing NBO is the most abundant.

The relationship between the CaO content and the coordination number of B–O interactions is shown in Fig. 9. From the graph, it can be observed that the coordination number of B-O interactions in glass falls within the range of 3.4-3.2, which is less than 3.5 (a coordination number of 3.5 means that tri- or tetra-coordinated boron are equal). This indicates that the content of ³B is consistently greater than that of 4B, which is consistent with the results obtained from ¹¹B-MAS-NMR in Fig. 5. Ohtori et al. [61] studied samples of xCaO· $(1-x)^{11}$ B₂O₃ (x = 0.20, 0.25, 0.33) glass and determined the coordination numbers of the first coordination shell of B–O interactions as follows: $CN_{B-O(ND)} \approx 3.11$, 3.18, 3.21 and $CN_{B-O(MD)} \approx 3.17$, 3.23, 3.28. Wright et al. [20] reported that the coordination number of B-O interaction in 0.28CaO·0.72B2O3 glass is 3.24. Their research findings closely align with our results. Therefore, the relative content has the order as ${}^{3}B-BO > {}^{4}B-BO > {}^{3}B-NBO$ > B-NBO, which is consistent with the results in Fig. 11. The change in the coordination number of the B–O interaction in Fig. 9 shows that the coordination number of the boron atom changes very little, which is consistent with the results obtained from ¹¹B-MAS-NMR shown in Fig. 5.

3.4.1.2. Ca–O interaction. As shown in Fig. 7, the Ca–O bond length r_{Ca-O} in the first coordination layer of calcium borate glass ranges from 2.37 to 2.40 Å. The r_{Ca-O} bond lengths of CaB₆O₁₀, CaB₄O₇, Ca₂B₆O₁₁, and CaB₂O₄ crystals are 2.37, 2.36, 2.44, and 2.38 Å, respectively, indicating that the Ca–O bond length of glass is close to that of crystal. The first peak of the Ca–O interaction of calcium borate glass is also asymmetric, primarily due to the interaction between calcium atoms and different types of oxygen atoms. By using atomic labeling, two types of oxygen atoms, BO and NBO, were labeled, and the Ca-BO and Ca-NBO interactions were shown in Fig. 12. The bond length and relative content of each interaction are shown in Table S8. From the graph, it can be observed that: (1) In the glass and crystals, the Ca-BO interaction

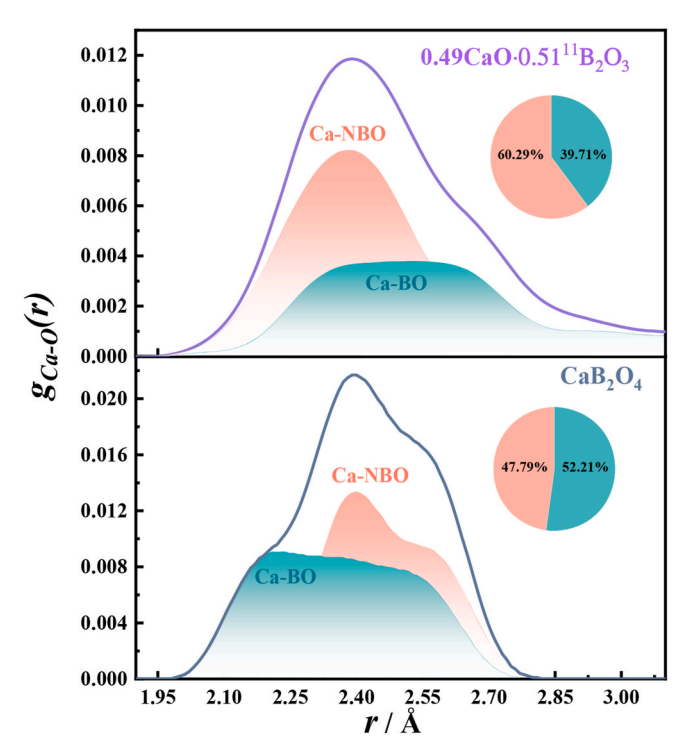


Fig. 12. The distribution of Ca-BO and Ca-NBO interactions in the first coordination layer of the Ca–O interaction in $0.49\text{Ca}O\cdot0.51^{11}B_2O_3$ glass and CaB_2O_4 crystal, the fan chart on the right shows the percentage of each atom-pair interaction.

exhibits a broad and blunt peak, while the Ca-NBO interaction has a relatively sharp peak with a shoulder on its right side. (2) In the glass, the Ca-BO bonds are noticeably longer compared to the Ca-BO bonds in the crystals of similar compositions. Similarly, the Ca-NBO bonds in the glass are shorter than the Ca-NBO bonds in the crystals of similar compositions. The relative content of Ca-NBO interaction in 0.49CaO·0.51 11 B₂O₃ glass and CaB₂O₄ crystal is 60.3 % and 47.8 % respectively, with bond lengths of 2.38 and 2.40 Å. In addition, the Ca-BO interaction in the glass has longer bond lengths compared to the crystals of similar compositions, and it also constitutes a smaller proportion. Above information indicates that the binding between Ca²⁺ and NBO in the glass is tighter. The glass contains both rings and chains structures, such as pyroborate and metaborate units with NBOs. Unlike the ring structure, the chain can be stretched and twisted to a certain extent, resulting in shorter Ca-NBO bond lengths in the glass.

Fig. 13 shows the relative contents of Ca-BO and Ca-NBO interaction in xCaO· $(1-x)^{11}$ B₂O₃ $(0.26 \le x \le 0.49)$ glass. When $0.26 \le x \le 0.40$, as the CaO content increases, the Ca-BO interaction gradually decreases, while the Ca-NBO interaction gradually increases. The above change is consistent with the changes in the content of BO and NBO shown in Fig. S11. When 0.40 < x < 0.49, the variation in the content of these two interactions is more complex. The main reason is that the six-membered rings and the metaborate-chains containing BØ₄ were transformed into pyroborate units and diborate groups (Fig. 2, right). In addition, when x = 0.42, the content of the two atoms interactions also change significantly, which is consistent with the turning point of the structural unit in the Raman spectrum (Fig. 2 right) and the B-O interaction (Fig. S11). This change is mainly caused by the change of pyroborate unit, diborate group, metaborate unit, etc. The schematic diagram in Fig. 13 represents a snapshot of the coordination of Ca²⁺ ions with an oxygen coordination number of 7 in 0.26CaO·0.74 11 B₂O₃ and 0.49CaO·0.51 11 B₂O₃ glass. In 0.26CaO·0.74 11 B₂O₃ glass, Ca²⁺ ions are mainly coordinated with BO units. However, in the 0.49CaO·0.51¹¹B₂O₃ system, Ca²⁺ ions primarily coordinate with NBO in both BO₃ and BØ₄ units. Kamitsos et al. 's [25]

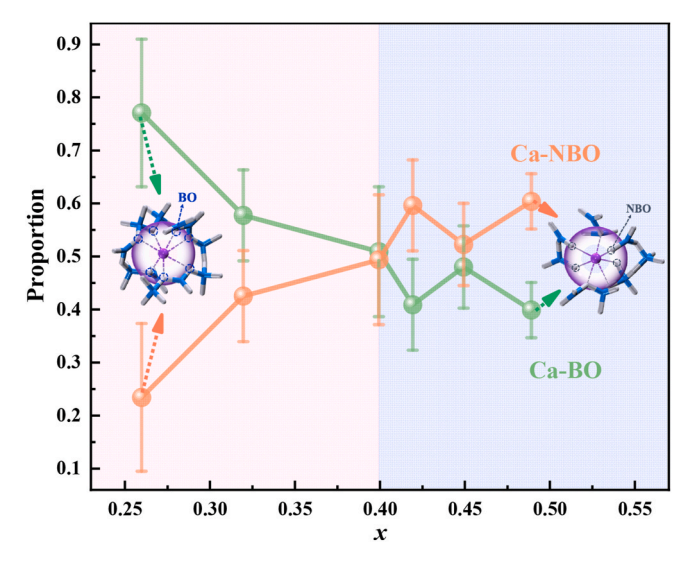


Fig. 13. The relative contents of Ca-BO and Ca-NBO interaction in xCaO- $(1-x)^{11}$ B₂O₃ $(0.26 \le x \le 0.49)$ glass.

study shows that there are L and H bands associated with ${\rm Ca}^{2+}$ vibration in the far-infrared spectral region of calcium borate glass, with L band corresponding to smaller electron density and H band corresponding to higher electron density. Consequently, the L band in the relatively low frequency region corresponds to the Ca-BO interaction, and the H band in the higher frequency region corresponds to the Ca-NBO interaction. This conclusion is very important for the analysis of far infrared spectra of borate glass.

Therefore, as the CaO content increases, the interaction between Ca^{2+} ions and NBOs increased, and the network structure of the glass was gradually destroyed. This leads to a reduction in the molar volume, an increase in solid-state density, and a decrease in the glass transition temperature of the glasses.

3.4.1.3. O-O interaction. The O-O distance $r_{\text{O-O}}$ is 2.42 Å. Ohtori et al. [61] suggested that the distance is 2.38 Å, which is close to the results of our study. As shown in Fig. 7 and S9, with an increase in the CaO content, the O-O interaction distance in the second coordination layer shifts to the right, indicating that the addition of CaO causes the O-O interactions to move towards medium-range order. It can be observed that the O-O interaction of the second coordination layer of the glass in this study is close to the O-NBO interaction in the crystal, so the O-O interaction of the second coordination layer is related to NBO. This indicates that with an increase in CaO content, the interactions associated with NBO also increase. This conclusion is consistent with the changes in NBO shown in Fig. S11. The O-O bond lengths in calcium borate glass are similar to those in the corresponding crystals, especially when x =0.25 and 0.32, where the O-O bond lengths in the corresponding crystals are almost the same as those in the glass. When x = 0.49, the distance between glass O-O bonds (2.42 Å) is close to the BO-NBO bonds (2.43 Å) in the CaB2O4 crystal. The coordination number of the O-O bonds in glass varies slightly in the range of 4.21-4.57, which is close to the coordination number of the crystals with similar composition. The above information shows that many NBOs are produced with the increase of CaO content, but the O-O interaction distance does not change significantly, so the coordination number changes little.

The distances and coordination numbers of the first coordination layer for B–B, Ca–B, and Ca–Ca interactions of the xCaO· $(1-x)^{11}$ B₂O₃ (0.26 \leq x \leq 0.49) glass are shown in Fig. 9, S9, and Table S5. In addition, the B–O–B angle distribution function analysis of calcium borate glass is shown in the B–O–B angle distribution function section of the SI section.

3.4.2. Ring analysis and cavity distribution of $xCaO \cdot (1-x)^{11}B_2O_3$ (0.26 $\leq x \leq 0.49$) glass

The rings distribution in xCaO· $(1-x)^{11}$ B₂O₃ $(0.26 \le x \le 0.49)$ glass is shown in Fig. 14 it shows that the number of rings gradually decreases when $0.26 \le x \le 0.40$. When $0.40 \le x \le 0.49$, the number of rings initially increases and then decreases, with the minimum number of rings is around x = 0.40. By combining the variations of structural units obtained from Raman spectroscopy (Fig. 2, right), when $0.26 \le x \le$ 0.40, boroxol ring and six-membered rings containing BØ4 tetrahedra transform into metaborate-chains, pyroborate units, and diborate groups. The change of the overall structural units shows that the content of ring structural units decreases, the content of "small molecular chain" structural units increases, and the structure becomes more dispersed. This change is consistent with the structural information in Fig. 14. When $0.40 \le x \le 0.49$, six-membered rings containing BØ₄ tetrahedra and metaborate-chains transform into pyroborate and diborate groups, resulting in an initial increase followed by a decrease of rings. Therefore, the extremum point of the variation in the content of ring structural units is also around x = 0.40, which is consistent with the information reflected in the ring distribution diagram (Fig. 14). The ring sizes distribution is shown in Fig. S13, where the predominant ring structure is the six-membered ring. As the CaO content increases, the variation of six-membered rings aligns with the overall change in the total number of rings. Apart from six-membered rings, there are eight-membered rings present in each component of calcium borate glass. Additionally, tenmembered and twelve-membered rings also appear as the majority of the structures of calcium borate glass. The types of ring structures contained in each component glass are shown in Fig. S14. As shown in the graph, there are six-membered double-ring structures connected by shared B atoms (pentaborate group, Figs. S14 and g) and six-membered double-ring structures connected by shared B-O bonds (Figs. S14 and f) in calcium borate glass. These two structures are also present in both lithium cesium borate and lithium borosilicate glass [32,62]. This may be a typical feature of metal-modified borate glass. It is also shown that the six-membered ring containing one BØ4 tetrahedrons obtained by Raman spectroscopy is a pentaborate group (Table S2).

The analysis of rings (Fig. S14) and chains (Fig. S15) structure shows that there are boroxol rings, six-membered rings containing one or two $B\varnothing_4$ tetrahedrons, diborate group, pentaborate group, pyroborate chains and metaborate chains in the calcium borate glass, which are consistent with the types of structural units obtained by Raman spectroscopy, and the change trend of ring structure is also close to the results of Raman (Fig. 2, right). In addition, AIMD simulation also obtained structures such as eight-membered rings, 10-membered rings, 12-membered rings, and complex six-membered three rings (Fig. S14) that Raman spectra could not give.

According to the center-based method [45], the micro cavity distribution of xCaO· $(1-x)^{11}$ B₂O₃ $(0.26 \le x \le 0.49)$ glass was calculated out as shown in Fig. 15. The cutoff radius for all components is 2.0 Å. With the increase of CaO content, the cavity occupancy of xCaO· $(1-x)^{11}$ B₂O₃ $(0.26 \le x \le 0.49)$ glass was 13.1 %, 11.8 %, 11.2 %, 10.1 %, 9.1 %, 9.0 %, and the cavity showed a gradually decreasing trend. With the increase of metal ions, there is also a decrease in void occupancy for sodium thioarsenate and silver thioarsenate glass [57,63,64]. The decrease in void occupancy is inversely proportional to the increase in density (Table 1). Fig. 16 shows the histogram of the cavity volume distribution in xCaO· $(1-x)^{11}$ B₂O₃ $(0.26 \le x \le 0.49)$ glass. When x = 0.26, the cavity volume primarily distributes at the minimum and maximum values, with cavity volumes of 8.5-51 Å³ and 239 Å³, respectively. The results of ring distribution (Fig. 14 and S13) also show that the relative content of ring structures is the highest, especially the boroxol ring. The boroxol ring does not exist in other components except x = 0.26 glass. Therefore, the more ring structure leads to the larger cavity occupancy. As the CaO content increases, the cavity distribution becomes increasingly uniform. In the xCaO· $(1-x)^{11}$ B₂O₃ (0.32 $\leq x \leq$ 0.49) glass, the cavity volumes range from 7 to 86 Å³. When x = 0.40, the cavities distribution of

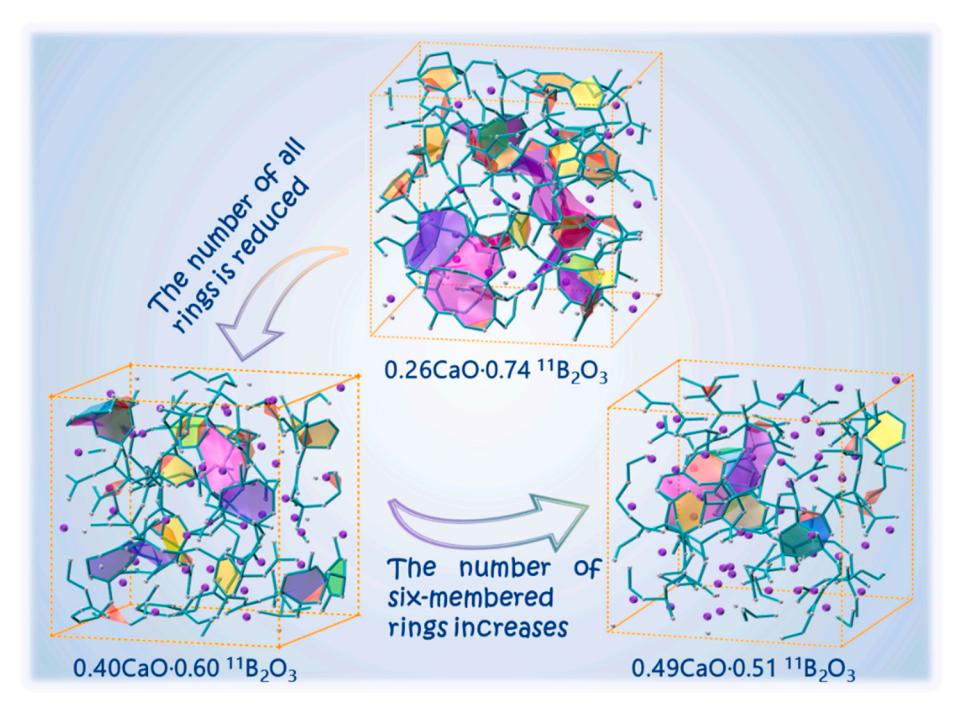


Fig. 14. Rings distribution in simulated box of xCaO·(1-x) 11 B₂O₃ (0.26 $\le x \le 0.49$) glass obtained by AIMD methods.

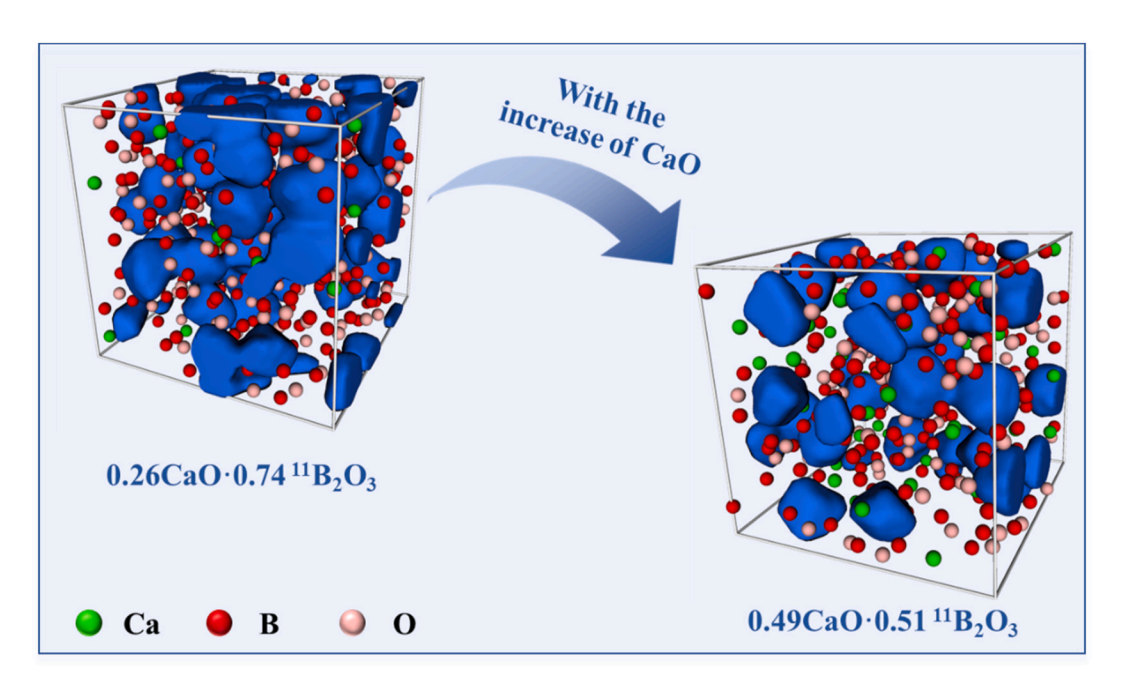


Fig. 15. The cavities distribution of xCaO·(1-x) 11 B₂O₃ $(0.26 \le x \le 0.49)$ glass.

different sizes is the most uniform. The ring analysis (Fig. 14, Supplementary Fig. 13) and Raman spectra (Fig. 2, right) in this component show that there is also a minimum point of ring content near x=0.40, so the reduction of rings will also lead to a more uniform distribution of void cavities in calcium borate glass.

3.5. The impact of structural changes on properties

The experimental density, reference density [65,66], atomic number density, molar volume, glass transition temperature, reference glass transition temperature [65], and similar composition crystals density of xCaO·(1-x)¹¹B₂O₃ (0.26 $\le x \le 0.49$) glass are shown in Fig. 17. We

believe that the structural factors and specific effects of this difference are as follows:

- (1) The N_4 of the crystal is always higher than that of the glass of similar composition (Fig. S10), and the increase in N_4 results in enhanced 3D boron-oxygen network connectivity and increased density. Therefore, we think that N_4 is the main factor influencing density.
- (2) Changes in structural units. The CaB_6O_{10} (x=0.25) crystal is primarily composed of six-membered rings containing one BO_4 tetrahedra. The CaB_4O_7 (x=0.33) crystal consists mainly of diborate groups. Both the $Ca_2B_6O_{11}$ (x=0.40) and CaB_2O_4 (x=0.40

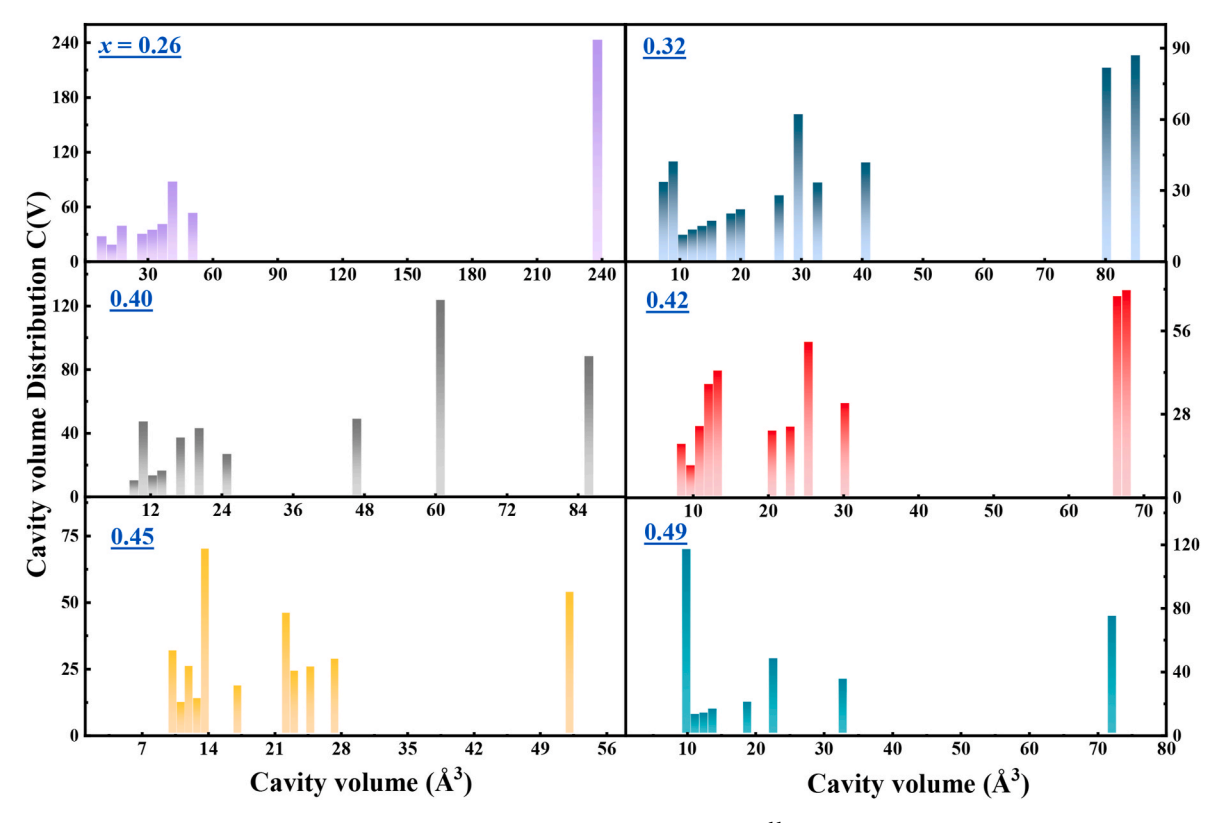


Fig. 16. The cavities volume distribution histogram of xCaO·(1-x) 11 B₂O₃ $(0.26 \le x \le 0.49)$ glass.

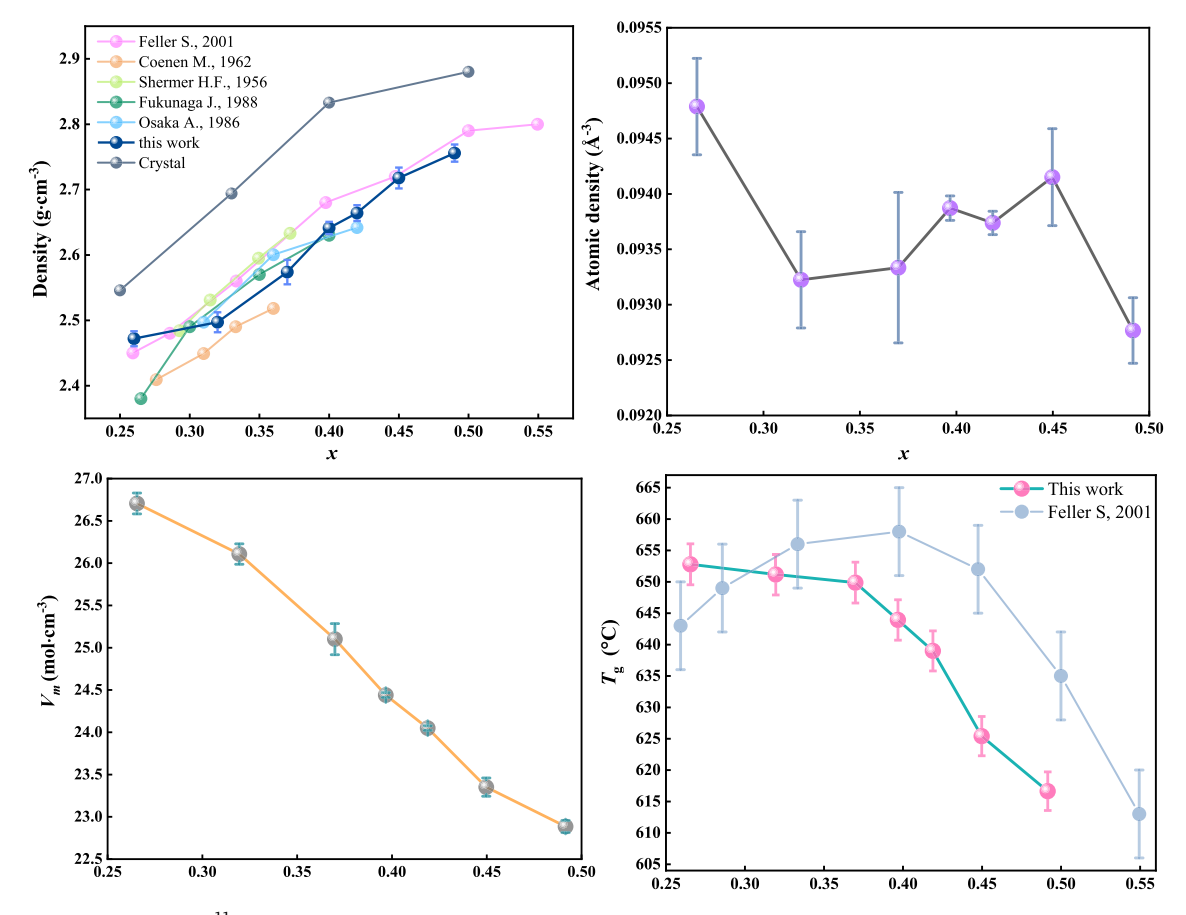


Fig. 17. Density data of xCaO· $(1-x)^{11}$ B₂O₃ $(0.26 \le x \le 0.49)$ glass and comparison with literature values [65,66], atomic number density, molar volume, glass transition temperature and comparison with literature values [65] curves.

0.50) crystals are composed of six membered rings containing two BØ $_4$ tetrahedra, but the CaB $_2$ O $_4$ (x=0.50) crystal also contains NBO. So, an increase in NBO leads to an increase in density. Singh et al. [67] have also shown that the increase in NBO results in a denser glass structure. The above information indicates that the increase in diborate groups and six-membered rings containing two BØ $_4$ tetrahedra leads to an increase in density. However, in addition to the ring structure of the above crystals, there are also chain structures that does not contain BØ $_4$ (such as pyroborate and metaborate chains) in the calcium borate glass. So, this may also be an important reason why the density of the glass is less than the crystal density.

With the increase of CaO content, N_3 and N_4 change little, the density of calcium borate glass increased, and the structural factors that cause the density change may include the following:

- (1) With the increase of CaO content, N_4 changed little, but NBO content increased gradually. Therefore, the increase of NBO is the main structural reason for the increase of calcium borate glass density.
- (2) From the perspective of the interaction of atomic pairs, Figs. 11 and 13 show that with the increase of CaO content at x < 0.4, the $^4\text{B-BO}$ interaction increases and the $^3\text{B-BO}$ interaction decreases, so the three-dimensional connectivity of the glass is enhanced. The bond length of $^3\text{B-NBO}$ and $^4\text{B-NBO}$ interactions is shorter than that of $^3\text{B-BO}$ and $^4\text{B-BO}$ interactions, respectively, so the structure becomes denser with the increase of $^3\text{B-NBO}$ and $^4\text{B-NBO}$ interactions, resulting in an increase in glass density. When 0.40 < x < 0.49, the changes of the interaction between atoms are relatively complex and need to be combined with the changes of structural units (Fig. 2, right) for analysis. In this range, the contents of diborate containing BØ4 and pyroborate containing NBO increase significantly, resulting in an increase in density.
- (3) With the increase of CaO content, the cavities occupancy of xCaO- $(1-x)^{11}B_2O_3$ (0.26 $\leq x \leq$ 0.49) glass gradually decreases, so the cavities occupancy is inversely proportional to the glass density.

In addition, the turning points of the structural unit change (x=0.32 and x=0.42) are also turning points of the change in the atomic density of the glass. With the increase of CaO content, the cavity occupancy of xCaO· $(1-x)^{11}$ B₂O₃ ($0.26 \le x \le 0.49$) glass gradually decreases, the NBO content gradually increases, and the glass transition temperature and molar volume both decrease gradually. Therefore, the cavity occupancy is proportional to the glass transition temperature and molar volume. The content of NBO is inversely proportional to the glass transition temperature and molar volume.

4. Conclusion

The main conclusions of the study on the *x*CaO· $(1-x)^{11}$ B₂O₃ (0.26 $\leq x \leq$ 0.49) glass structure are as follows:

- (1) The increase of CaO content mainly leads to the conversion of BO to NBO in the glass microstructure, and also promotes the mutual conversion between BO₃ and BØ₄, but has little effect on the relative contents of BO₃ and BØ₄ in the glass.
- (2) As the content of NBO increases, the interaction between Ca-NBO and B-NBO increases. Interestingly, the bond length distribution of Ca-NBO and B-NBO is shorter than that of Ca-BO and B-BO, so the glass structure becomes denser.
- (3) There are three main structural factors that affect the properties of glass:
- 1) Atomic type. The increase of BØ₄ and NBO content contribute to an increase in glass density and decrease in the glass transition temperature. 2) Structural units. the change of atomic density

and structural unit have the same turning points 3) Cavity occupancy rate. The cavity occupancy rate is inversely proportional to the glass density and directly proportional to the T_{φ} and V_{m} .

Declaration of competing interest

The authors declare that they have no known competing financial interests or personal relationships that could have appeared to influence the work reported in this paper.

Acknowledgements

We thank the Natural Science Foundation of Qinghai (No. 2020–HZ–811), Qinghai Province "High-end Innovative Talents Plan" (E240HX1001) and the US National Science Foundation (DMR-RUI 2203142) project for financial support. We also thank the China Spallation Neutron Source (CSNS) for beam-time on Multi-physics instrument MPI (No. P1621080100053)

Appendix A. Supplementary data

Supplementary data to this article can be found online at https://doi.org/10.1016/j.ceramint.2023.11.412.

References

- T.N.H. Tengku Kamarul Bahri, H. Wagiran, R. Hussin, I. Hossain, T. Kadni, Thermoluminescence properties of CaO–B2O3 glass system doped with GeO2, Radiat, Phys. Chem. 102 (2014) 103–107.
- [2] R. Shafaghi, O. Rodriguez, A.W. Wren, L. Chiu, E.H. Schemitsch, P. Zalzal, S. D. Waldman, M. Papini, M.R. Towler, In vitro evaluation of novel titania-containing borate bioactive glass scaffolds, J. Biomed. Mater. Res. 109 (2021) 146–158.
- [3] S.B. Jung, Borate Based Bioactive Glass Scaffolds for Hard and Soft Tissue Engineering, Missouri University Of Science And Technology, Missouri, 2010.
- 4] N.J. Thyparambil, L.C. Gutgesell, B.A. Bromet, L.E. Flowers, S. Greaney, D.E. Day, J.A. Semon, Bioactive borate glass triggers phenotypic changes in adipose stem cells, J. Mater. Sci. Mater. Med. 31 (2020) 35.
- [5] J. Zhou, H. Wang, S. Zhao, N. Zhou, L. Li, W. Huang, D. Wang, C. Zhang, In vivo and in vitro studies of borate based glass micro-fibers for dermal repairing, Mater. Sci. Eng. C 60 (2016) 437–445.
- [6] Y. Lin, R.F. Brown, S.B. Jung, D.E. Day, Angiogenic effects of borate glass microfibers in a rodent model, J. Biomed. Mater. Res. 102 (2014) 4491–4499.
- [7] B. Gupta, J.B. Papke, A. Mohammadkhah, D.E. Day, A.B. Harkins, Effects of chemically doped bioactive borate glass on neuron regrowth and regeneration, Ann. Biomed. Eng. 44 (2016) 3468–3477.
- [8] K.A. Cole, G.A. Funk, M.N. Rahaman, T.E. McIff, Characterization of the conversion of bone cement and borate bioactive glass composites, J. Biomed. Mater. Res. 108 (2020) 1580–1591.
- [9] H.A. Tajuddin, W.M.S. WanHassan, S.F.A. Sani, N.S. Shaharin, Thermoluminescent properties of Dy doped calcium borate based glass for dose measurement subjected to photon irradiation, EPJ Web Conf. 156 (2016), 00002.
- [10] J. Huang, L. Zhou, Q. Pang, F. Gong, J. Sun, W. Wang, Photoluminescence properties of a novel phosphor CaB2O4:Eu3+ under NUV excitation, Luminescence 24 (2009) 363–366.
- [11] K. Machida, G. Adachi, J. Shiokawa, M. Shimada, M. Koizumi, High-pressure synthesis, characterization, and properties of europium(II) metaborate and europium(II)-activated strontium and calcium metaborates, Inorg. Chem. 19 (1980) 983–992.
- [12] R. Bhimireddi, P.W. Jaschin, K. Mishra, A.A. Ansari, Luminescence properties of CaMoO4 nanoparticles embedded borate composite glass, J. Solid State Chem. 302 (2021), 122400.
- [13] J. Krogh-Moe, Structural interpretation of melting point depression in the sodium borate symstem, Phys. Chem. Glasses 3 (1962) 101–110.
- [14] P.J. Bray, Structural models for borate glasses, J. Non-Cryst. Solids 75 (1985) 29–36.
- [15] P.J. Bray, Nuclear magnetic resonance studies of glass structure, J. Non-Cryst. Solids 73 (1985) 19–45.
- [16] Y. Yu, B. Stevensson, M. Edén, Direct experimental evidence for abundant BO4–BO4 motifs in borosilicate glasses from double-quantum 11B NMR spectroscopy, J. Phys. Chem. Lett. 9 (2018) 6372–6376.
- [17] V. Montouillout, H. Fan, L. del Campo, S. Ory, A. Rakhmatullin, F. Fayon, M. Malki, Ionic conductivity of lithium borate glasses and local structure probed by high resolution solid-sate NMR, J. Non-Cryst. Solids 484 (2018) 57–64.
- [18] J.R. Berryman, S.A. Feller, M. Affatigato, M. Kodama, B.M. Meyer, S.W. Martin, F. Borsa, S. Kroeker, Thermal, acoustic, and nuclear magnetic resonance studies of cesium borate glasses, J. Non-Cryst. Solids 293 (2001) 483–489.

- [19] S.G. Bishop, P.J. Bray, Nuclear magnetic resonance studies of calcium boroaluminate glasses, Phys. Chem. Glasses 7 (1966) 73-81.
- A.C. Wright, R.N. Sinclair, C.E. Stone, J.L. Shaw, S.A. Feller, T. Kiczenski, R. B. Williams, H.A. Berger, H.E. Fischer, N.M. Vedishcheva, A neutron diffraction study of 2M2O. 5B2O3 (M= Li, Na, K, Rb, Cs & Ag) and 2MO. 5B2O3 (M= Ca & Ba) glasses, Phys. Chem. Glasses: Eur. J. Glass Sci. Technol. B. 53 (2012) 191-204.
- [21] N. Ohtori, K. Takase, I. Akiyama, Y. Suzuki, K. Handa, I. Sakai, Y. Iwadate, T. Fukunaga, N. Umesaki, Short-range structure of alkaline-earth borate glasses by pulsed neutron diffraction and molecular dynamics simulation, J. Non-Cryst. Solids 293-295 (2001) 136-145.
- [22] N. Ohtori, K. Takase, I. Akiyama, K. Handa, Y. Iwadate, N. Umesaki, MD study of the short range structure of RO. xB2O3 glasses: R= Mg, Ca, Sr and Ba; x= 1, 2, 3 and 4, J. Phys. Chem. B 41 (2000) 369-372.
- [23] E.I. Kamitsos, Infrared studies of borate glasses, Phys. Chem. Glasses 44 (2003)
- [24] D. Maniu, T. Iliescu, I. Ardelean, S. Cinta-Pinzaru, N. Tarcea, W. Kiefer, Raman study on B2O3-CaO glasses, J. Mol. Struct. 651-653 (2003) 485-488.
- [25] Y.D. Yiannopoulos, G.D. Chryssikos, E.I. Kamitsos, Structure and properties of alkaline earth borate glasses, Phys. Chem. Glasses 42 (2001) 164-172.
- [26] T. Ohkubo, E. Tsuchida, T. Takahashi, Y. Iwadate, Ab initio molecular dynamics simulations and GIPAW NMR calculations of a lithium borate glass melt, J. Phys. Chem. B 120 (2016) 3582-3590.
- [27] R.E. Youngman, J.W. Zwanziger, Network modification in potassium borate glasses: structural studies with NMR and Raman spectroscopies, J. Phys. Chem. C 100 (1996) 16720–16728.
- [28] S.A. Feller, W.J. Dell, P.J. Bray, ¹⁰B NMR studies of lithium borate glasses, J. Non-Cryst. Solids 51 (1982) 21-30.
- [29] P.J. Bray, NMR studies of the structures of glasses, J. Non-Cryst. Solids 96 (1987)
- [30] K.I. Chatzipanagis, N.S. Tagiara, E.I. Kamitsos, N. Barrow, I. Slagle, R. Wilson, T. Greiner, M. Jesuit, N. Leonard, A. Phillips, Structure of lead borate glasses by Raman, ¹¹B MAS, and ²⁰⁷Pb NMR spectroscopies, J. Non-Cryst. Solids 589 (2022), 121660.
- [31] L.S. Du, J.F. Stebbins, Nature of Silicon-Boron mixing in sodium borosilicate glasses: a high-resolution 11B and 17O NMR study, J. Phys. Chem. B 107 (2003) 10063-10076.
- [32] T. Ohkubo, S. Urata, Y. Imamura, T. Taniguchi, N. Ishioka, M. Tanida, E. Tsuchida, L. Deng, J. Du, Modeling the structure and dynamics of lithium borosilicate glasses with ab initio molecular dynamics simulations, J. Phys. Chem. C 125 (2021) 8080-8089.
- [33] J. Xu, Y. Xia, Z. Li, H. Chen, X. Wang, Z. Sun, W. Yin, Multi-physics instrument: total scattering neutron time-of-flight diffractometer at China spallation neutron Source, nucl. Instrum, Methods Phys. Res. 1013 (2021), 165642.
- [34] O. Arnold, J.-C. Bilheux, J. Borreguero, A. Buts, S.I. Campbell, L. Chapon, M. Doucet, N. Draper, R.F. Leal, M. Gigg, Mantid—data analysis and visualization package for neutron scattering and μ SR experiments, Nucl. Instrum. Methods Phys. Res. 764 (2014) 156-166.
- [35] D. Massiot, F. Favon, M. Capron, I. King, S. Le Calve, B. Alonso, J.O. Durand, B. Bujoli, Z.H. Gan, G. Hoatson, Modelling one- and two-dimensional solid-state NMR spectra, Magn. Reson. Chem. 40 (2002) 70-76.
- [36] J. Hutter, M. Iannuzzi, F. Schiffmann, J. VandeVondele, CP2K: atomistic simulations of condensed matter systems, WIREs Comput. Mol. Sci. 4 (2014) 15 - 25
- [37] Z. Wu, R.E. Cohen, More accurate generalized gradient approximation for solids, J. Phys. Rev. B 73 (2006), 235116.
- [38] L. Martínez, R. Andrade, E.G. Birgin, J.M. Martínez, PACKMOL: a package for building initial configurations for molecular dynamics simulations, J. Comput. Chem. 30 (2009) 2157-2164.
- [39] J. VandeVondele, J. Hutter, Gaussian basis sets for accurate calculations on molecular systems in gas and condensed phases, J. Chem. Phys. 127 (2007), 114105.
- [40] D.V. Oliveira, J. Laun, M.F. Peintinger, T. Bredow, BSSE-correction scheme for consistent Gaussian basis sets of double- and triple-zeta valence with polarization quality for solid-state calculations, J. Comput. Chem. 40 (2019) 2364-2376.
- S. Goedecker, M. Teter, J. Hutter, Separable dual-space Gaussian pseudopotentials, Phys. Rev. B 54 (1996) 1703.
- S. Nosé, A molecular dynamics method for simulations in the canonical ensemble, Mol. Phys. 52 (1984) 255-268.
- [43] W.G. Hoover, Canonical dynamics: equilibrium phase-space distributions, Phys. Rev. A. 31 (1985) 1695.

- [44] S. Le Roux, P. Jund, Ring statistics analysis of topological networks: new approach and application to amorphous GeS2 and SiO2 systems, Comput. Mater. Sci. 49 (2010) 70-83.
- [45] I. Heimbach, F. Rhiem, F. Beule, D. Knodt, J. Heinen, R.O. Jones, pyMolDyn: identification, structure, and properties of cavities/vacancies in condensed matter and molecules, J. Comput. Chem. 38 (2017) 389-394.
- [46] A.K. Soper, Partial structure factors from disordered materials diffraction data: an approach using empirical potential structure refinement, J. Phys. Rev. B 72 (2005), 104204.
- [47] E.I. Kamitsos, A. Karakassides, G.D. Chryssikost, Vibrational spectra of magnesiumsodium-borate glasses. 2. Raman and mid-infrared investigation of the network structure, J. Phys. Chem. 91 (1987) 1073-1079.
- [48] B.N. Meera, J. Ramakrishna, Raman spectral studies of borate glasses, J. Non-Cryst. Solids 159 (1993) 1-21.
- E.I. Kamitsos, M.A. Karakassides, G.D. Chryssikost, A vibrational study of Lithium borate glasses with high Li2O content, Phys. Chem. Glasses 28 (1987) 203-209.
- [50] E.I. Kamitsos, M.A. Karakassides, G.D. Chryssikos, Structure of borate glasses. Part 1. Raman study of caesium, rubidium, and potassium borate glasses, Phys. Chem. Glasses 30 (1989) 229-234.
- [51] L.L. Song, Y.X. Wang, A.C. Hannon, S. Feller, W. Li, Y.Q. Zhou, F.Y. Zhu, Structural investigation of lithium borate glasses by Raman spectroscopy: quantitative evaluation of structural units and its correlation with density, J. Non-Cryst. Solids 616 (2023), 122478.
- [52] T. Takaishi, J. Jin, T. Uchino, T. Yoko, Structural study of PbO-B2O3 glasses by Xray diffraction and 11B MAS NMR techniques, J. Am. Ceram. Soc. 83 (2000)
- [53] J.F. Stebbins, P. Zhao, S. Kroeker, Non-bridging oxygens in borate glasses: characterization by 11B and 17O MAS and 3QMAS NMR, Solid State Nucl. Magn. Reson. 16 (2000) 9-19.
- [54] S. Feller, T. Mullenbach, M. Franke, S. Bista, A. O'Donovan-Zavada, K. Hopkins, D. Starkenberg, J. McCoy, D. Leipply, J. Stansberry, Structure and properties of barium and calcium borosilicate glasses, Phys. Chem. Glasses: Eur. J. Glass Sci. Technol. B. 53 (2012) 210-218.
- [55] A.A. Osipov, L.M. Osipova, Raman scattering study of barium borate glasses and melts, J. Phys. Chem. Solid. 74 (2013) 971-978.
- [56] J. Yang, I. Sohn, Compositional dependence of thermophysical properties in binary alkaline earth borate melts: insights from structure in short-range and intermediate-range order, J. Mater. Sci. Technol. 131 (2022) 195-203.
- [57] M. Kassem, T. Bounazef, D. Fontanari, A. Sokolov, M. Bokova, A.C. Hannon, E. Bychkov, Chemical and structural variety in sodium thioarsenate glasses studied by neutron diffraction and supported by first-principles simulations, Inorg. Chem. 59 (2020) 16410-16420.
- [58] A.C. Hannon, XTAL Structural Modelling Software, 2023, http://www.alexhannon. co.uk/.
- [59] A.C. Hannon, XTAL, A Program for Calculating Interatomic Distances and Coordination Numbers for Model Structures, Rutherford Appleton Laboratory Report RAL-93-063, 1993.
- [60] F.A. Akeroyd, R.L. Ashworth, S.I. Campbell, S.D. Johnston, C.M. Moreton-Smith, R. G. Sergeant, D.S. Sivia, Open Genie Reference Manual, Rutherford Appleton Laboratory Report RAL-TR-1999-031, 1999
- [61] Y. Suzuki, N. Ohtori, K. Takase, K. Handa, K. Itoh, T. Fukunaga, N. Umesaki, Pulsed neutron diffraction studies of RO center dot xB2O3 glasses: R=Ca, Sr and Ba; x=2, 3 and 4, Phys. Chem. Glasses 44 (2003) 150-154.
- [62] S. Kojima, Mixed-alkali effect in borate glasses: thermal, elastic, and vibrational properties, Solids 1 (2020) 16-30.
- J. Akola, P. Jóvári, I. Kaban, I. Voleská, J. Kolář, T. Wágner, R.O. Jones, Structure, electronic, and vibrational properties of amorphous AsS2 and AgAsS2: experimentally constrained density functional study, Phys. Rev. B 89 (2014), 064202.
- [64] J. Akola, B. Beuneu, R.O. Jones, P. Jóvári, I. Kaban, J. Kolář, I. Voleská, T. Wágner, Structure of amorphous Ag/Ge/S alloys: experimentally constrained density functional study, J. Phys. Condens. Matter 27 (2015), 485304.
- N.P. Lower, J.L. McRae, H.A. Feller, A.R. Betzen, S. Kapoor, M. Affatigato, S. A. Feller, Physical properties of alkaline-earth and alkali borate glasses prepared over an extended range of compositions, J. Non-Cryst. Solids 293 (2001) 669–675. [66] SciGlass Professional 7.3, ITC Inc., 2008.
- V. Dua, S.K. Arva, K. Singh, Review on transition metals containing lithium borate glasses properties, applications and perspectives, J. Mater. Sci. 58 (2023) 8678-8699.